





SHOTGLAS

II. MUSE spectroscopy of blue horizontal branch stars in the core of ω Centauri and NGC 6752^{★,★★}

M. Latour¹ , S. Hämmerich² , M. Dorsch^{3,2} , U. Heber², T.-O. Husser¹, S. Kamman⁴,
S. Dreizler¹, and J. Brinchmann^{5,6} 

- ¹ Institut für Astrophysik und Geophysik, Georg-August-Universität Göttingen, Friedrich-Hund-Platz 1, 37077 Göttingen, Germany
e-mail: marilyn.latour@uni-goettingen.de
² Dr. Karl Remeis-Observatory and Erlangen Centre for Astroparticle Physics, Friedrich-Alexander-Universität Erlangen-Nürnberg,
Sternwartstr. 7, 96049 Bamberg, Germany
³ Institut für Physik und Astronomie, Universität Potsdam, Haus 28, Karl-Liebknecht-Str. 24/25, 14476, Potsdam-Golm, Germany
⁴ Astrophysics Research Institute, Liverpool John Moores University, IC2 Liverpool Science Park, 146 Brownlow Hill, Liverpool,
L3 5RF, UK
⁵ Leiden Observatory, Leiden University, PO Box 9513, 2300 RA Leiden, The Netherlands
⁶ Instituto de Astrofísica e Ciências do Espaço, Universidade do Porto, CAUP, Rua das Estrelas, 4150-762 Porto, Portugal

Received 5 April 2023 / Accepted 23 June 2023

ABSTRACT

Aims. We want to study the population of blue horizontal branch (HB) stars in the centres of globular clusters (GC) for the first time by exploiting the unique combination of MUSE spectroscopy and HST photometry. In this work, we characterize their properties in the GCs ω Cen and NGC 6752.

Methods. We use dedicated model atmospheres and grids of synthetic spectra computed using a hybrid LTE/NLTE modeling approach to fit the MUSE spectra of HB stars hotter than 8000 K in both clusters. The spectral fits provide estimates of the effective temperature (T_{eff}), surface gravity ($\log g$), and helium abundance of the stars. The model grids are further used to fit the HST magnitudes of the stars, that is, their spectral energy distributions (SEDs). From the SED fits, we derive the average reddening, radius, luminosity, and mass of the stars in our sample.

Results. The atmospheric and stellar properties that we derive for the stars in our sample are in good agreement with theoretical expectations. In particular, the stars cooler than $\sim 15\,000$ K closely follow the theoretical predictions on radius, $\log g$, and luminosity for helium-normal ($Y = 0.25$) models. In ω Cen, we show that the majority of these cooler HB stars cannot originate from a helium-enriched population with $Y > 0.35$. The properties of the hotter stars (radii and luminosities) are still in reasonable agreement with theoretical expectations, but the individual measurements show a large scatter. For these hot stars, we find a mismatch between the effective temperatures indicated from the MUSE spectral fits and the photometric fits, with the latter returning T_{eff} lower by ~ 3000 K. We use three different diagnostics, namely the position of the G-jump and changes in metallicity and helium abundances, to place the onset of diffusion in the stellar atmospheres at T_{eff} between 11 000 and 11 500 K. Our sample includes two stars known as photometric variables; we confirm one to be a bona fide extreme HB object but the other is a blue straggler star. Finally, unlike what has been reported in the literature, we do not find significant differences between the properties (e.g., $\log g$, radius, and luminosity) of the stars in the two clusters.

Conclusions. We show that our analysis method – combining MUSE spectra and HST photometry of HB stars in GCs – is a powerful tool for characterising their stellar properties. With the availability of MUSE and HST observations of additional GCs, we have a unique opportunity to combine homogeneous spectroscopic and photometric data to study and compare the properties of blue HB stars in different GCs.

Key words. stars: fundamental parameters – stars: horizontal-branch – globular clusters: individual: NGC 5139 – globular clusters: individual: NGC 6752

1. Introduction

Globular clusters (GCs) may be considered ideal laboratories for studying stellar evolution. However, evidence is mounting that they are not simple stellar populations. Multiple stellar populations have been discovered on the main sequence (MS) and/or red giant branch (RGB), showing up as distinct sequences in the color–magnitude diagrams (CMDs) of numerous Galactic GCs, most prominently in massive clusters such as ω Cen and NGC 2808. However, the formation mechanisms for these

* Tables B.1–B.6 are available at the CDS via anonymous ftp to cdsarc.cds.unistra.fr (130.79.128.5) or via <https://cdsarc.cds.unistra.fr/viz-bin/cat/J/A+A/677/A86>

** Based on observations collected at the European Organisation for Astronomical Research in the Southern Hemisphere, Chile (Program IDs 094.D-0142(B), 095.D-0629(A), 096.D-0175(A), 097.D-0295(A), 098.D-0148(A), 099.D-0019(A), 0100.D-0161(A), 0101.D-0268(A), 0102.D-0270(A), 0103.D-0204(A), 0104.D-0257(B), and 105.20CR.002).

multiple populations remain unclear (see [Renzini et al. 2015](#); [Bastian & Lardo 2018](#)). Peculiarities have also been found when comparing the morphology of the horizontal branches (HBs) of GCs in CMDs, such as the “second parameter” problem. It became obvious that the HB morphology of GCs is not determined by metallicity alone. Other parameters such as age, helium abundance, and many others have been suggested to explain the HB star distributions in the cluster CMDs (see e.g., [Recio-Blanco et al. 2006](#); [Moehler 2001](#); [Catelan 2009](#); [Miocchi 2007](#); [Dotter et al. 2010](#)). Traditionally, the HB is divided into a red and a blue part separated by the RR Lyrae instability strip at ~ 8000 K. Discontinuities along the HBs are ubiquitous for clusters with extended blue HBs, such as the “Grundahl jump” (G-jump) at $\sim 11\,500$ K ([Grundahl et al. 1999](#)), the “Moman jump” (M-jump) separating the bluest “extreme” HB (EHB) at $\sim 20\,000$ K from the blue HB (BHB)¹; [Moman et al. 2002](#); [Newell 1973](#); [Newell & Graham 1976](#)). Finally, there is the gap between the EHB and “blue-hook” stars, which was first identified by [D’Cruz et al. \(2000\)](#) in ω Cen and later found in the most massive clusters near $\sim 32\,000$ – $36\,000$ K ([Brown et al. 2010](#); [Moehler 2010](#)). Discrete main sequences and RGBs may be linked to the HB morphology and discontinuities ([Yi 2008](#)).

HB stars burn helium in their cores, and those that are sufficiently massive ($M \gtrsim 0.55 M_{\odot}$) also sustain hydrogen-shell burning. They are the progeny of low-mass RGB stars ([Hoyle & Schwarzschild 1955](#); [Faulkner 1966](#)). Generally, the mass of the helium-burning core ($\sim 0.5 M_{\odot}$) is the same across the entire sequence. However, the mass of the hydrogen envelope surrounding the core is different, making the HB a sequence of hydrogen-envelope mass. The envelope mass decreases with increasing effective temperature (T_{eff}), the HB is therefore also a temperature sequence. Consequently, the atmospheric structure is fundamentally different along the HB ([Dorman 1992](#); [Brown et al. 2016](#)). The structural and atmospheric changes along the HB manifest themselves as the gaps and discontinuities mentioned above.

BHB stars have a wide spread of temperatures (from 8000 K to $20\,000$ K) and are mainly found in two spectral classes. The A-type BHB stars (A-BHB) cover temperatures between 8000 K and $11\,500$ K, meaning that they are cooler than the G-jump. Helium abundances of A-BHBs are at the solar level ([Adelman & Philip 1996](#); [Kinman et al. 2000](#); [Behr 2003](#)) and the metal abundances are consistent with what is observed within the respective cluster population. This chemical homogeneity is maintained by atmospheric convection and multiple subsurface convection zones driven by the ionization of hydrogen and helium ([Caloi 1999](#); [Sweigart 2002](#); [Brown et al. 2016](#)). With increasing effective temperatures, these zones are pushed towards the surface and disappear at $\sim 11\,500$ K, which also marks the transition to the B-type BHB stars (B-BHB). Due to the lack of atmospheric convection zones, B-BHBs have radiative atmospheres, which also give rise to atomic diffusion (radiative levitation versus gravitational settling; see e.g., [Hui-Bon-Hoa et al. 2000](#); [Quievy et al. 2009](#); [Michaud et al. 2011](#)). Due to radiative levitation, heavy metals (e.g., iron) are enriched and high metal abundances are found among B-BHBs ([Behr 2003](#); [Pace et al. 2006](#)). However, the helium abundance steadily decreases with temperature, which is due to gravitational settling, reaching a minimum at $\sim 15\,000$ K ([Moni Bidin et al. 2012](#)). At even higher effective temperatures, the He abundance increases again but remains subsolar. At a temperature of

about $20\,000$ K, the hydrogen-envelope mass has decreased to a level no longer supporting hydrogen-shell burning. The last convection zone from He II encroaches upon the surface near this temperature and ceases to exist in the hotter stars ([Brown et al. 2016](#)). [Brown et al. \(2017\)](#) found that the stars hotter than the M-jump in ω Cen have lower Fe abundances than their colder counterparts. It is these changes, happening at about $18\,000$ – $20\,000$ K, that are believed to be responsible for the M-jump in the CMD of GCs. These hotter stars on the blue side of the M-jump form the extreme (or extended) horizontal branch (EHB). In the Galactic field, the EHB stars are also referred to as hot subdwarfs, with spectral types B and O (sdB and sdO, [Heber 2009, 2016](#)).

While many hot subdwarf stars in the field are known to be close binaries with periods of hours to days ([Maxted et al. 2001](#); [Copperwheat et al. 2011](#)), only very few such binaries have been found in GCs ([Moni Bidin et al. 2008](#); [Moni Bidin 2018](#)), including NGC 6752 ([Moni Bidin et al. 2006](#)). A population of binary subdwarfs explains the excess UV emission observed for elliptical galaxies ([Han et al. 2007](#)) and the UV colours of early-type galaxies in the Virgo cluster ([Lisker & Han 2008](#)). [Pelisoli et al. \(2020\)](#) concluded that binary evolution is required to explain the origin of all types of hot subdwarfs amongst the field population. In this scenario, the single subdwarfs result from mergers of helium white dwarfs ([Han et al. 2002, 2003](#)). The lack of binaries in GCs could result from the much larger merger fraction than in the field ([Han 2008](#)). The mass distribution of hot subdwarfs resulting from mergers is predicted to be much wider than that of binary subdwarfs and to contain subdwarfs more massive than those in close binaries ([Han et al. 2003](#)). Consequently, the mass distribution of GC subdwarfs should be wide, with masses from 0.3 up to $0.9 M_{\odot}$. Hence, it is of great importance to accurately determine the masses of sufficiently large samples of EHB (subdwarf) and BHB stars in GCs. This could allow us to test whether or not BHBs and EHBs form in different ways (single vs. binary evolution).

In this investigation, we analyse a spectral dataset of blue HB stars (bluer than the RR Lyrae gap) in two GCs: ω Cen and NGC 6752. These two clusters have an extended and well-populated blue HB. Because the clusters are also nearby, their HB stars are relatively bright and they have been extensively studied in the past. Spectroscopic investigations include [Heber et al. \(1986\)](#), [Moehler et al. \(1997, 1999, 2000\)](#), and [Moni Bidin et al. \(2007\)](#) for NGC 6752, and [Moehler et al. \(2002, 2007, 2011\)](#), [Moni Bidin et al. \(2012\)](#), and [Latour et al. \(2014, 2018\)](#) for ω Cen. The EHB of NGC 6752 hosts stars with T_{eff} up to $\sim 30\,000$ K that are depleted in helium, these EHB stars are the counterparts to the field sdBs.

In addition to the EHB, ω Cen also harbors a blue-hook population that extends at magnitudes fainter than the canonical EHB. The blue-hook stars in ω Cen are hotter than $30\,000$ K and are also enriched in He and C compared to the EHB stars.

Previous ground-based spectroscopic investigations, such as the first paper of this series ([Latour et al. 2018](#)), targeted HB stars found in the outskirts of the clusters where crowding is not a severe issue. The previous investigations listed above used low- to medium-resolution (0.7 – 2.6 \AA) spectra obtained with various instruments (FLAMES, FORS, VIMOS) at the Very Large Telescope (VLT) to derive atmospheric parameters (T_{eff} , $\log g$, He). In some cases, masses were also estimated, mostly using bolometric corrections as in [Moehler et al. \(2011\)](#). In this work, we use spectra collected as part of the MUSE GC survey ([Kamann et al. 2018](#), P.I.: S. Dreizler, S. Kamann) to gather a large and homogeneous sample of HB stars located in the

¹ BHB stars are hotter than the RR Lyrae instability strip but cooler than the EHB.

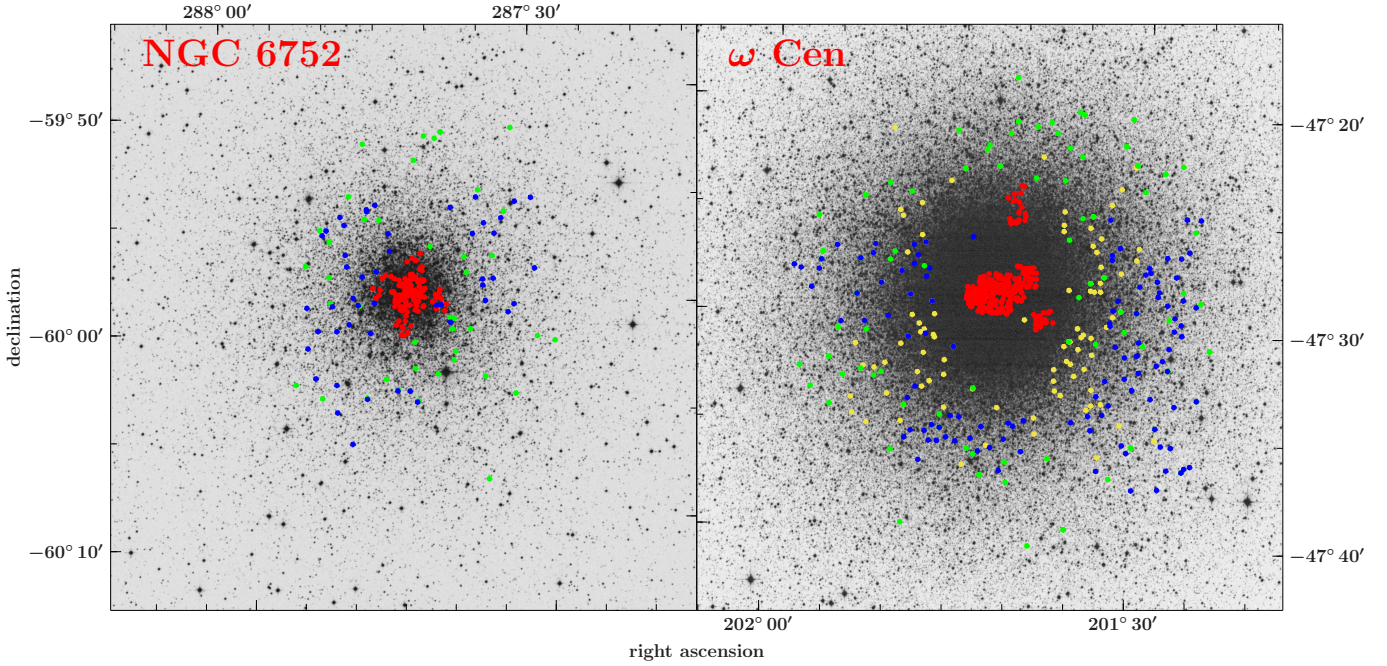


Fig. 1. Positions of the HB stars observed by MUSE in both GCs, shown in red. Left panel: ω Cen. Right panel: NGC 6752. The positions of the stars analyzed in previous studies are also indicated. Moehler et al. (2011, green), Moni Bidin et al. (2012, blue), and Latour et al. (2018, yellow) are shown for ω Cen and Moehler et al. (1997, green) and Moni Bidin et al. (2007, blue) are shown for NGC 6752. The images are from the Digitized Sky Survey. (Copyright by Anglo-Australian Observatory/the Royal Observatory Edinburgh.)

central regions of ω Cen and NGC 6752 (see Fig. 1). Atmospheric parameters are derived from the MUSE spectra using state-of-the-art model atmospheres. The majority of the stars in our samples are located within the *Hubble* Space Telescope (HST) footprint and have magnitudes published as part of catalogs in several HST filters. We used our own model atmospheres to construct and fit the spectral energy distributions (SEDs) of the stars. Because the distances and reddening to the clusters are well constrained and the atmospheric parameters of the stars are known from the MUSE spectra, the SED fits allow us to derive stellar parameters – namely the radius, luminosity, and mass – with unprecedented precision. The parameters derived are then compared to evolutionary models.

The paper is organized as follows. The MUSE observations and data processing are described in Sect. 2. In Sect. 3, we present the model atmospheres and synthetic spectra used (Sect. 3.1) followed by a detailed description of our analysis methods for the spectral fits (Sects. 3.2–3.4). The analysis of the SEDs based on the HST photometry is presented in Sect. 3.5. The final samples for both clusters are presented in Sect. 4. Our resulting atmospheric parameters are discussed at length in Sect. 5 where we present our samples in various parameter planes (e.g., $T_{\text{eff}} - \log g$ and $T_{\text{eff}} - \text{helium}$) and compare them with theoretical models and literature results. Section 6 presents our results for two variable stars (V16 and V17) and four hot blue straggler stars (BSSs) in NGC 6752. Our SED fit results, in terms of radius, luminosity, and mass are presented and discussed in Sect. 7. Section 8 presents a comparison of the two clusters. Finally, we summarize our results and conclude in Sects. 9 and 10.

2. MUSE observations

We used the Multi Unit Spectroscopic Explorer (MUSE; Bacon et al. 2010) GTO observations of ω Cen and NGC 6752 obtained

in wide field mode ($1' \times 1'$) between April 2014 and May 2022. The observations from 2018 to 2022 benefitted from the use of the adaptive optics system installed on UT4 of the VLT. A total of ten and eight $1' \times 1'$ fields were observed in ω Cen and NGC 6752, respectively. These fields include the most central and crowded regions of the cluster (see Fig. 1), where the use of an integral field spectrograph is particularly efficient. A summary of the MUSE observations is presented in Table 1.

The spectra cover the 4750–9350 Å range with an average spectral resolution of ~ 2.5 Å ($R \sim 3000$), although this varies slightly across the wavelength range (Husser et al. 2016). This range is redder than what is normally used to study HB stars; it only includes the two Balmer lines H_α and H_β . However, the Paschen lines from H_{3-9} to the Paschen jump are covered. The data reduction is done with the standard MUSE pipeline (Weilbacher et al. 2020) and a general description of the different steps is presented in Kamann et al. (2018). The stellar spectra are extracted with the PAMPELMUSE software (Kamann et al. 2013; Kamann 2018), which relies on the existence of a photometric catalog. We used HST catalogs to identify the sources present in the field of view and deblend the individual spectra (Sarajedini et al. 2007; Anderson et al. 2008). We use the photometry of Anderson & van der Marel (2010) for the spectral extraction of stars in the external fields (6–11 in Table 1) of ω Cen because these regions are not fully covered by the Anderson et al. (2008) catalog.

Each field of view was observed at multiple epochs, and therefore the individual spectra were co-added to obtain the final, high signal-to-noise (S/N) spectrum. Each individual spectrum is fitted with synthetic spectra from the Göttingen spectral library of PHOENIX models (Husser et al. 2013). This grid only covers effective temperatures up to 15 kK, but the goal is to achieve a fit that is good enough to provide a radial velocity (v_r) and to reproduce the telluric lines. This allows the individual spectra to

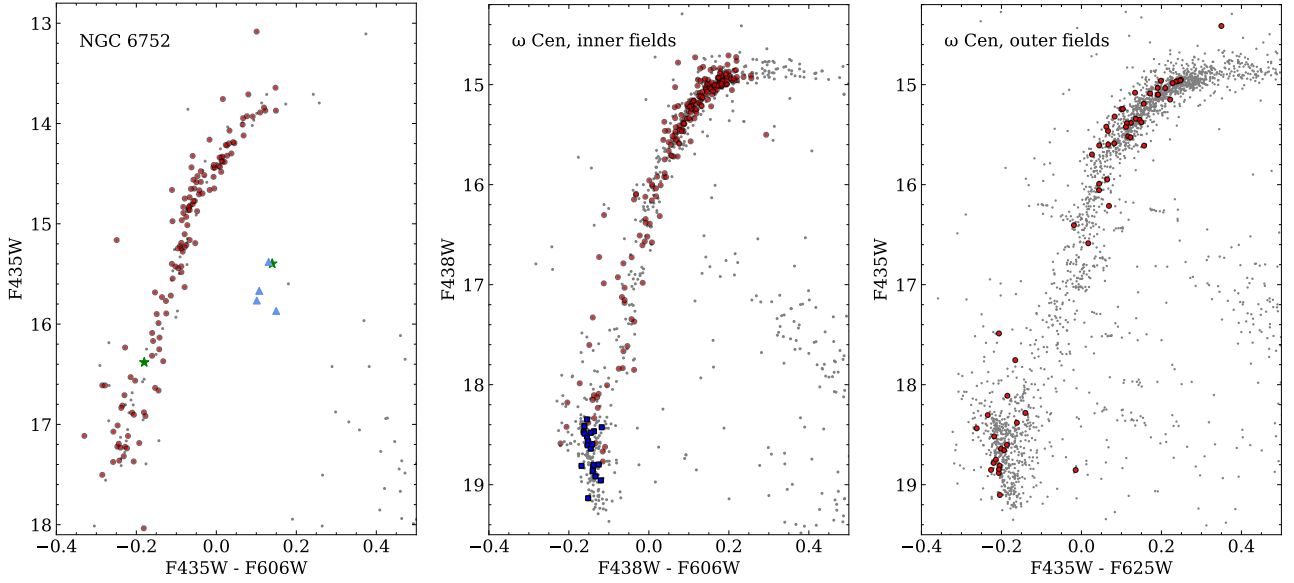


Fig. 2. Optical CMDs of NGC 6752 and ω Cen. The stars included in the spectroscopic samples are identified with large red dots. NGC 6752: also shown are the variable stars V16 and V17 (stars) and the four bright blue stragglers (triangles). The magnitudes are from the HUGS survey (Nardiello et al. 2018). ω Cen: the blue-hook stars in ω Cen are marked with blue squares. The magnitudes for the central fields of view (1 to 6 in Table 1) are from the catalog of Bellini et al. (2017a) and the magnitudes for stars in the outer fields (7, 8, 11, and 12) are from Anderson & van der Marel (2010).

Table 1. MUSE observations of ω Cen and NGC 6752.

Field	RA	Dec	# Epochs		Total exp. time (s)
			non-AO	AO	
ω Cen					
1	13:26:45.0	−47:29:09	8	7	2025
2	13:26:45.0	−47:28:24	7	7	1890
3	13:26:49.5	−47:29:09	7	10	2250
4	13:26:49.5	−47:28:24	7	10	2295
5	13:26:40.6	−47:28:31	7	7	3280
6	13:26:53.1	−47:29:01	7	10	4080
7	13:26:36.8	−47:27:54	6	9	4500
8	13:26:31.0	−47:29:55	7	9	7200
11	13:26:40.3	−47:25:00	6	8	12 600
12	13:26:47.2	−47:24:03	4	8	21 600
NGC 6752					
1	19:10:49.10	−59:59:26.84	2	1	1080
2	19:10:49.12	−59:58:41.84	2	1	1080
3	19:10:55.10	−59:59:26.95	2	1	1080
4	19:10:55.12	−59:58:41.95	2	1	1080
11	19:11:04.29	−59:58:41.19	1	2	3000
12	19:10:39.13	−59:59:29.03	0	9	17 400
13	19:10:48.62	−59:57:37.58	0	2	2000
14	19:10:55.35	−60:00:38.19	0	2	2000

be shifted to restframe velocity, to have the telluric absorption removed, and to be co-added. More details on this procedure are presented in Husser et al. (2016) with the main difference that for HB stars, the surface gravity is fitted along with T_{eff} . Their work also presents the case of the sdO star ROB 162 in NGC 6397 (Heber & Kudritzki 1986), showing that the hydrogen lines are reproduced surprisingly well with a colder model, in this case that of an F-type star. This example shows that the v_r ,

and telluric lines can be corrected for in stars hotter than 15 kK, even if the best-fit solution is not realistic².

The final, co-added, telluric-free spectra are then fitted with proper model atmospheres as described in Sect. 3. In general, the S/N decreases with increasing magnitude but is also strongly dependent on the number of individual spectra that were collected. This depends on the position of the star in the cluster, that is, in which field of view it is located, and whether it is found in an overlapping region between two fields. We initially selected stars based on their positions in the CMD. Our final samples of stars in both clusters, described in greater detail in Sect. 4, are shown in their respective CMDs in Figs. 2 and 3.

3. Analysis method

3.1. Model atmospheres and synthetic spectra

The model atmospheres and synthetic spectra used in this work were computed using the so-called ADS approach. ADS is a hybrid LTE/NLTE method (local thermodynamic equilibrium and non-local thermodynamic equilibrium), which was first described by Przybilla et al. (2006) and Nieva & Przybilla (2007), and has since been improved by various authors (Przybilla et al. 2011; Irrgang et al. 2014, 2018b). This approach is consistent with results achieved by means of full NLTE methods for hot stars ($T_{\text{eff}} \lesssim 35$ kK, Przybilla et al. 2011). The calculation is done using the procedure described in Irrgang et al. (2018b) and Kreuzer et al. (2020). The final synthetic spectra are obtained by subsequently running three different codes. At first, an LTE line-blanketed, plane-parallel, homogeneous, and hydrostatic model atmosphere is calculated using ATLAS12 (Kurucz 1996). The resulting LTE atmospheric structure is then used by

² In the future, we plan to further improve our data reduction method by using our HB synthetic spectral grids, described in Sect. 3.1, to fit individual spectra and remove the telluric absorption before combination, instead of the Phoenix models.

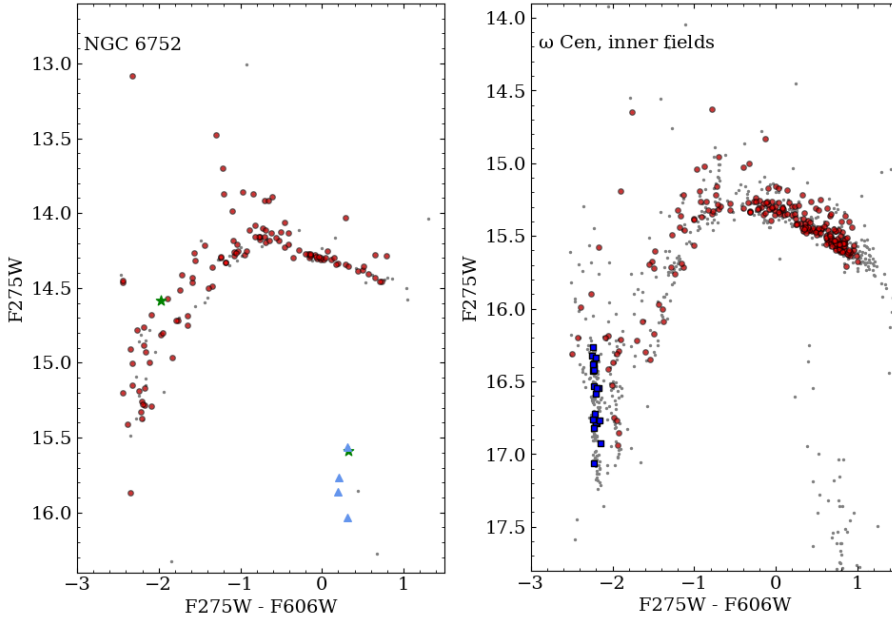


Fig. 3. F275W–F606W CMD of NGC 6752 and ω Cen. Symbols are the same as in Fig. 2.

DETAIL (Giddings 1981; Butler & Giddings 1985) to calculate the population numbers of hydrogen (Przybilla & Butler 2004) and helium (Przybilla 2005) assuming NLTE and using appropriate model atoms. Other chemical elements are considered, assuming a scaled solar abundance pattern (Asplund et al. 2009) in ATLAS12 and DETAIL as background opacities. The NLTE population numbers of H and He are then used in ATLAS12 to obtain a refined atmospheric structure (Irrgang et al. 2018a). The process of passing the NLTE population numbers between the two codes is repeated until convergence is reached. The final model atmosphere is then used by SURFACE (Giddings 1981; Butler & Giddings 1985) to compute a synthetic spectrum including lines of hydrogen and helium. In this process, we use the occupation probability formalism (Hummer & Mihalas 1988) for H and He by Hubeny et al. (1994) and the line-broadening data of Tremblay & Bergeron (2009) for hydrogen. For the most recent improvements of the code, see Irrgang et al. (2021, 2022).

We note that our models are calculated without microturbulence. We computed five overlapping grids of model atmospheres and synthetic spectra in order to cover the whole parameter range of the blue HB stars in terms of T_{eff} , $\log g$, and helium abundance. The helium abundance is given as the logarithm of the fractional particle number with respect to all particles, which we denote $\log N(\text{He})/N(\text{tot})$. The surface gravity is varied in steps of 0.2 dex and the helium abundance in steps of 0.25 dex. We used solar-scaled chemical mixtures to produce model atmospheres at metallicities $[M/H]^3$ between -2.0 and 0.5 in steps of 0.5 dex. The steps in T_{eff} are not uniform across all grids. The coverage of the individual grids is listed in Table 2.

3.2. Spectral fitting procedure

Spectral fitting is carried out using the Interactive Spectral Interpretation System (ISIS; Houck & Denicola 2000) with a modified version of the χ^2 -minimization method presented by Irrgang et al. (2014). To normalize the observed spectra, the continuum is modeled using a spline with anchor points

Table 2. Properties of the model grids.

Grid #	T_{eff} (K)	T_{eff} step (K)	$\log g$ (cm s^{-1})	$\log N(\text{He})/N(\text{tot})$
1	8000–12 500	250	2.4–4.4	–5.0 to –0.50
2	11 000–17 000	250	2.8–6.0	–5.0 to –0.25
3	15 000–26 000	1000	3.0–6.4	–5.0 to –0.25
4	22 000–40 000	1000	4.0–6.6	–5.0 to –0.25
5	38 000–55 000	1000	4.6–6.6	–5.0 to –0.25

placed every 100 Å while avoiding the hydrogen and helium lines. The spectral region containing the interstellar NaD lines (5882.0–5901.0 Å) is excluded. During the fitting process, the resolving power (R) of MUSE is considered to be a linear function, where the resolution increases with the observed wavelength. The equation for R was obtained from fitting the value of R at different wavelengths from the fit of the hydrogen lines. The macroturbulence and projected rotational velocity are set to 0 km s^{-1} . A low projected rotational velocity is fully consistent with what is expected for HB stars in general (Geier & Heber 2012; Hämmerich 2020). For A-BHB stars, $v \sin i$ are expected to be below 40 km s^{-1} (see, e.g., Behr 2003). Given the low spectral resolution of MUSE, and considering that we are fitting broad hydrogen lines, such a $v \sin i$ has no measurable effect on the resulting atmospheric parameters. The model spectra are convolved with a Gaussian following the relationship between R and λ , and linear interpolation within the grid is used to determine the best-fit atmospheric parameters.

Every fit is first carried out using the lowest temperature grid (#1). If the resulting T_{eff} is within 4% of the grid’s upper limit, the fitting procedure is performed again using the following grid with a higher temperature. Once the best solution within a grid is found, wavelength regions with metal lines and artifacts are identified using 3σ outliers in the χ^2 and are ignored as well (however regions around the hydrogen and helium lines are protected in this procedure) in order to ensure an appropriate fit. Afterwards, the fit is repeated not taking the ignored regions into account. Based on χ^2 statistics, statistical errors are calculated by

³ $[M/H] = \log(M/H) - \log(M/H)_{\odot}$.

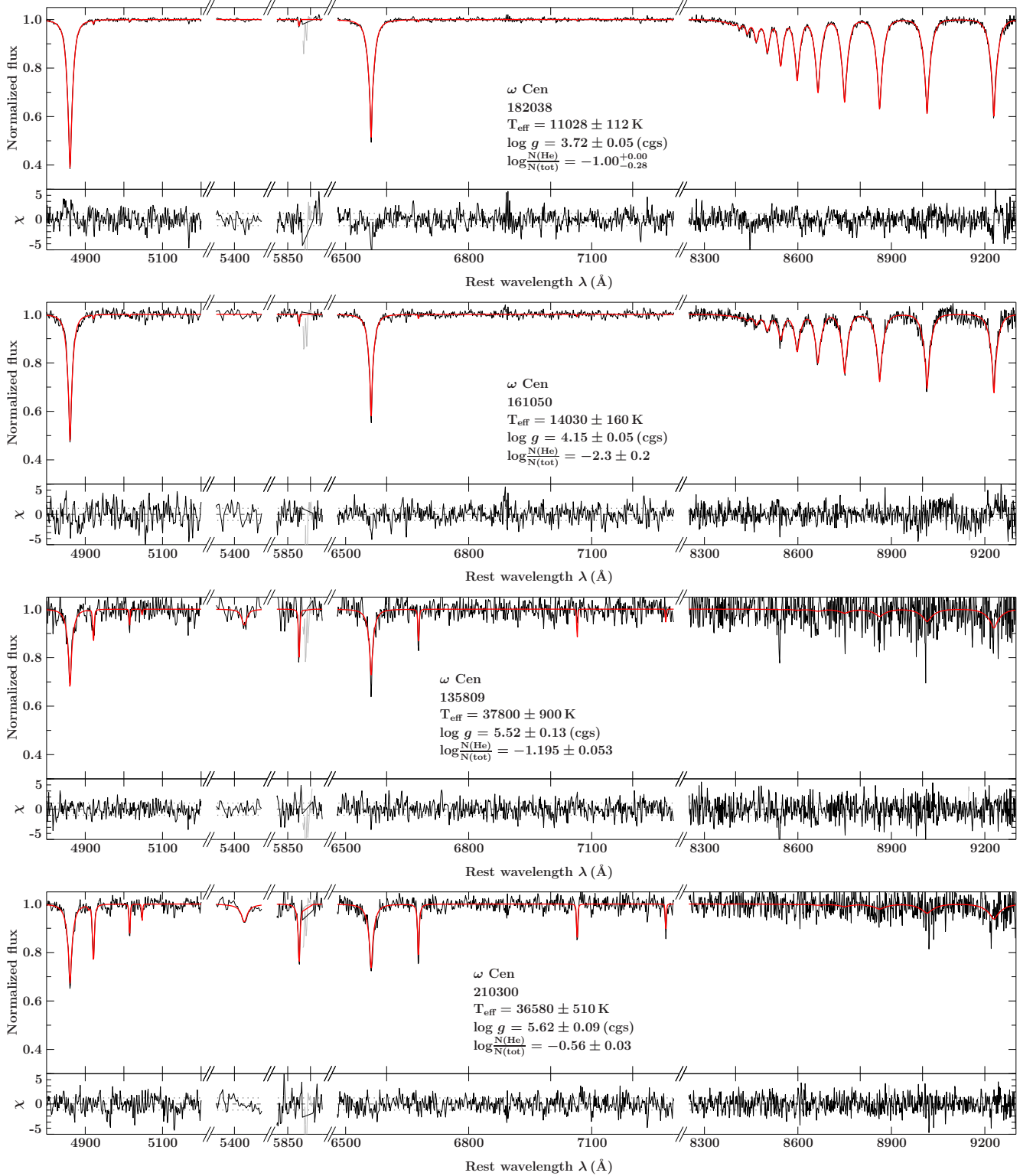


Fig. 4. Examples of spectroscopic fits for stars in ω Cen. Best fit (red) to the normalized spectrum (black) of, from top to bottom, an A-BHB, B-BHB, EHB, and blue-hook star. The residuals are shown below each fit. Only the regions with spectral lines of hydrogen and helium are plotted. The cluster name, star identification number, and resulting spectral parameters are indicated for each fit.

computing the confidence limits (68%) as presented in [Irrgang et al. \(2014\)](#). Systematic errors are considered as well, assuming an uncertainty of 1% in T_{eff} and 0.04 dex for the surface gravity. The final uncertainties are given as the quadratic sum of the systematic and statistical uncertainties. The radial velocity v_{rad} is left as a free parameter in order to account for possible deviations

from 0 km s^{-1} , the velocity to which the spectra were shifted in the combination process.

Example fits of various stars along the HB in both clusters are shown in Figs. 4 and 5. Certain factors are important to keep in mind after the examination of these figures. The S/N generally decreases with increasing temperature because the hotter stars

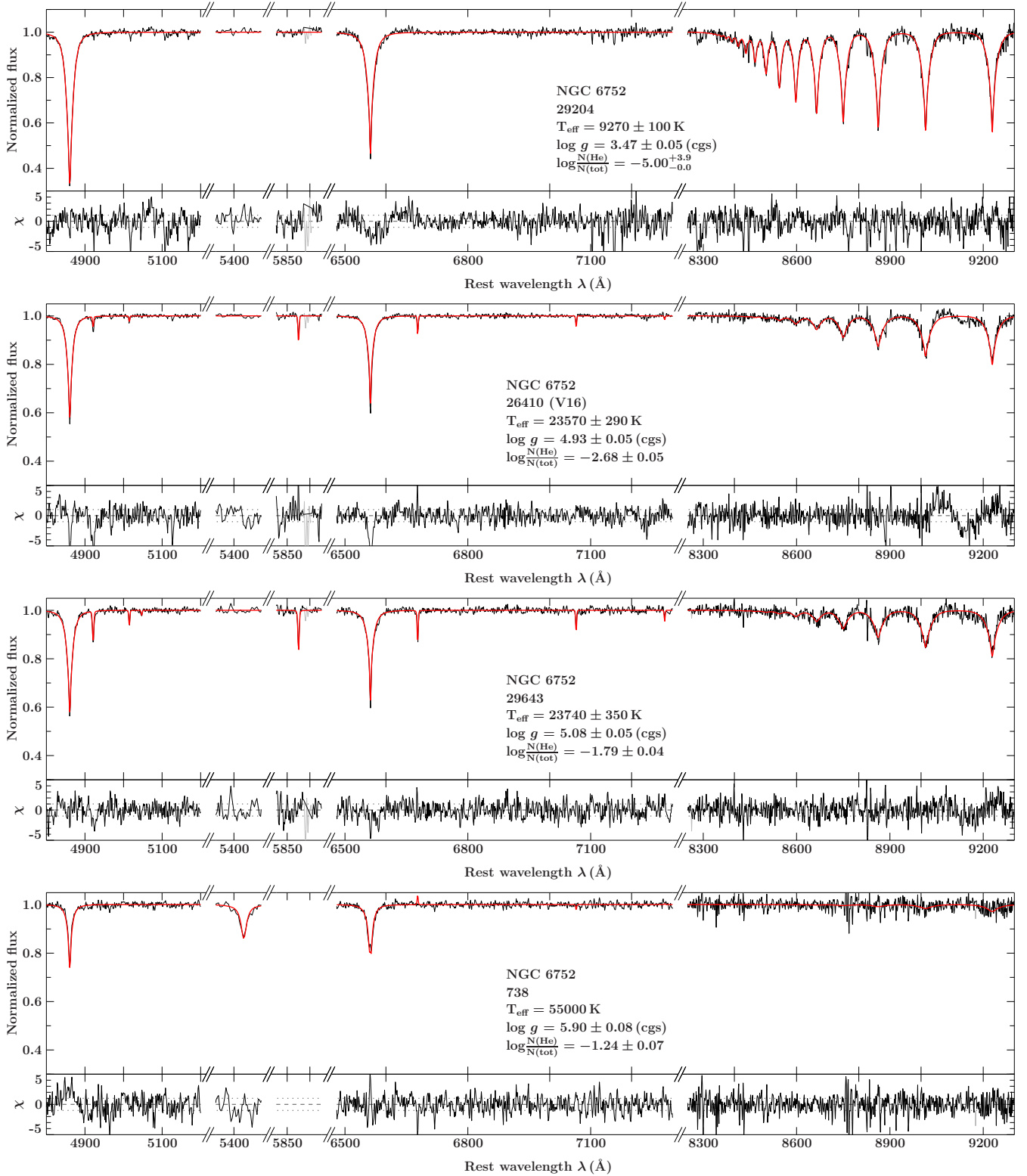


Fig. 5. Same as Fig. 4 but for stars in NGC 6752. From top to bottom, an A-BHB, V16, an EHB with similar T_{eff} to V16, and the hot post-EHB (H-sdO) star. Star 738 was only observed with AO, hence the gap in the Na D lines region.

are fainter. The number and strength of the hydrogen lines also decrease with increasing temperature because hydrogen is ionized. This means that with the MUSE spectra, we expect the atmospheric parameters to be less precise for the hot stars. As extreme examples, we show in Fig. 4 the fits of a low S/N spectrum (135809, $S/N \approx 20$) and in Fig. 5 the fit of the hottest star

(738) in NGC 6752. In the latter case, the fit reached the border of the model grid at 55 kK. We have a few such hot stars in our samples, and we are aware that the T_{eff} of these objects is a rough estimate, but we can nevertheless state that they are likely to have T_{eff} larger than 50 kK and we assign them an H-sdO spectral type (see Latour et al. 2018 for the different spectral types of

EHB stars). The Paschen lines are prominent in the A-BHB and B-BHB stars and these lines provide a good constraint on the surface gravity. However, the strength and the number of Paschen lines diminish as hydrogen is ionized in the hot objects. In stars hotter than ~ 30 kK, these lines often vanish in the noise.

3.3. Treatment of helium

In the cooler stars ($T_{\text{eff}} \lesssim 11$ kK), the helium lines are very weak and usually not visible in the MUSE spectra. Some studies have shown that helium abundances in these A-BHB stars are consistent with the solar value (Adelman & Philip 1996; Kinman et al. 2000; Behr 2003; Villanova et al. 2009, 2012; Marino et al. 2014). This is also in line with the fact that the stars cooler than the G-jump have convective atmospheres. This is why, in previous studies, the helium abundance was fixed to the solar value for A-BHB stars (see, e.g., Moni Bidin et al. 2007). To assess the impact of fixing the helium abundance on the fits and resulting atmospheric parameters, we used sets of synthetic spectra with solar helium abundance and fitted them in the MUSE spectral range while keeping the helium abundance fixed to different values (from $\log N(\text{He})/N(\text{tot}) = -3.0$ to -0.5). These tests revealed that the assumed helium abundance influences the resulting atmospheric parameters significantly, with differences of up to 400 K in T_{eff} and 0.4 dex in $\log g$. This indicates that the helium abundance, even when helium lines are weak or not visible, has an impact on the hydrogen lines that are used as temperature and surface-gravity indicators. Therefore, we performed our fits with the helium abundance as a free parameter for the whole temperature range with the only constraint that the maximum helium value is set to the solar abundance in the cool stars ($T_{\text{eff}} < 11.5$ kK). However, the fact that the helium lines are weak in these stars is reflected in the large uncertainties obtained for their He abundance.

3.4. Treatment of metallicity

As mentioned in Sect. 1, the stars along the HB do not have the same atmospheric composition because of the onset of diffusion at ~ 11.5 kK. In ω Cen, the intrinsic metallicity and abundance spreads within the cluster are also likely to affect the atmospheric composition of the HB stars. We fitted all stars with the $[M/H] = -1.5$ grid and with the $[M/H] = 0$ (solar metallicity) grid. For stars colder than the G-jump, meaning those with a convective atmosphere, we keep the results obtained with the $[M/H] = -1.5$ models; this metallicity is in agreement with the mean metallicity of both clusters. For the hotter stars, where diffusion changes the atmospheric composition, we keep the results obtained with the solar metallicity grid. The use of solar metallicity is a crude yet reasonable estimate. The element-to-element abundances resulting from diffusion are more complex but most of the atomic species become more abundant under the effect of radiative levitation (Behr 2003; Brown et al. 2017; Michaud et al. 2011). Our analysis of the SED of the stars in ω Cen further supports this conclusion (see Sect. 3.5). Using a metallicity that is as appropriate as possible in the model atmospheres adopted for the spectral fits is important because, as for the helium abundance, $[M/H]$ influences the resulting parameters. To quantify this, we compared the T_{eff} and $\log g$ obtained from our fits with the $[M/H] = 0$ and -1.5 models. The differences in $\log g$ are at most ± 0.1 dex. In terms of T_{eff} , for the A-BHB stars, the difference is up to 200 K, while it reaches 1000 K in the EHB stars at $\sim 20\,000$ K.

3.5. Spectral energy distribution and stellar parameters

To complete our analysis, we derive mass, radius, and luminosity for the stars in our samples. This is done by fitting the SED of the stars defined by their magnitude at different wavelengths and making use of the known distances of the clusters. We construct grids of synthetic fluxes in the various HST filters from our ATLAS12 model atmosphere grids. A general description of the SED fitting method used for field sdBs is presented in Heber et al. (2018).

For NGC 6752, we used the magnitudes provided in the five filters available from the HST UV Globular Cluster Survey (HUGS): ACS/WFC $F435W$, $F606W$, $F814$, and WFC3/UVIS $F275W$, $F336W$ (Piotto et al. 2015; Nardiello et al. 2018)⁴. For ω Cen, we use eight WFC3/UVIS magnitudes from the catalog of Bellini et al. (2017a)⁵ ($F225W$, $F275W$, $F336W$, $F390W$, $F438W$, $F555W$, $F606W$, $F775W$, $F814W$) and the ACS/WFC $F435W$ and $F625W$ magnitudes of Anderson & van der Marel (2010). The error on the magnitudes is computed by adding in quadrature the error provided in the catalogs (the RMS of individual measurements) when available, and a systematic uncertainty, of typically 0.01–0.02 mag, related to the photometric calibration zero points. The uncertainties for T_{eff} and $\log g$ come from the spectroscopic fits, but we add in quadrature 0.08 dex to the $\log g$ error. This stems from our previous experiences in fitting spectra of hot subdwarf and BHB stars.

We adopt a distance of $D = 4.125 \pm 0.04$ kpc and $D = 5.43 \pm 0.05$ kpc for NGC 6752 and ω Cen, respectively (Baumgardt & Vasiliev 2021). With the distance to the GCs fixed, the parameters that influence the shape of the SED are the angular diameter Θ ($= 2R/D$), the interstellar reddening $E(44-55)$ ⁶, T_{eff} , $\log g$, metallicity, and, to a lesser extent, the helium content of the model atmospheres. The surface gravity and helium abundance cannot be well constrained by photometry, and so we used the spectroscopic values obtained from the MUSE spectra. The metallicity is fixed in the same way as for the spectroscopic analysis (see the previous subsection).

We account for interstellar extinction using the functions of Fitzpatrick et al. (2019) and adopt a ratio of total-to-selective extinction of $R(55) = 3.02$, which is the Milky Way average. Because we realized that the results are sensitive to the adopted reddening $E(44-55)$, the SED fits were performed in two iterations. In the first step, we leave the reddening and Θ as free parameters while T_{eff} is fixed to its spectroscopic value. We then used the reddening obtained for the stars colder than 13 kK – for which the spectroscopic and photometric effective temperatures are in good agreement – to derive an average reddening for each cluster (see Appendix A for additional details). As a result, we obtained $E(44-55) = 0.041$ mag for NGC 6752 and 0.119 mag for ω Cen. We note that these values are in excellent agreement with the literature (Harris 1996, 2010 edition). The second step is to perform the final fit with $E(44-55)$ fixed to the values mentioned above and T_{eff} and Θ left as free parameters. From Θ , we directly obtain the radius of the star because the distances to the clusters (D) are well known. We compute the luminosity and the mass

⁴ <https://archive.stsci.edu/prepds/hugs/>

⁵ We note that for both the HUGS and Bellini et al. (2017a) data we used the Method 1 catalogs.

⁶ $E(44-55)$ is analogous to $E(B-V)$, but with the monochromatic measures of the extinction at 4400 and 5500 Å substituting for measurements with the B and V filters. Conversion factors to the UBV systems are given in Table 4 of Fitzpatrick et al. (2019). They are close to 1 for hot stars.

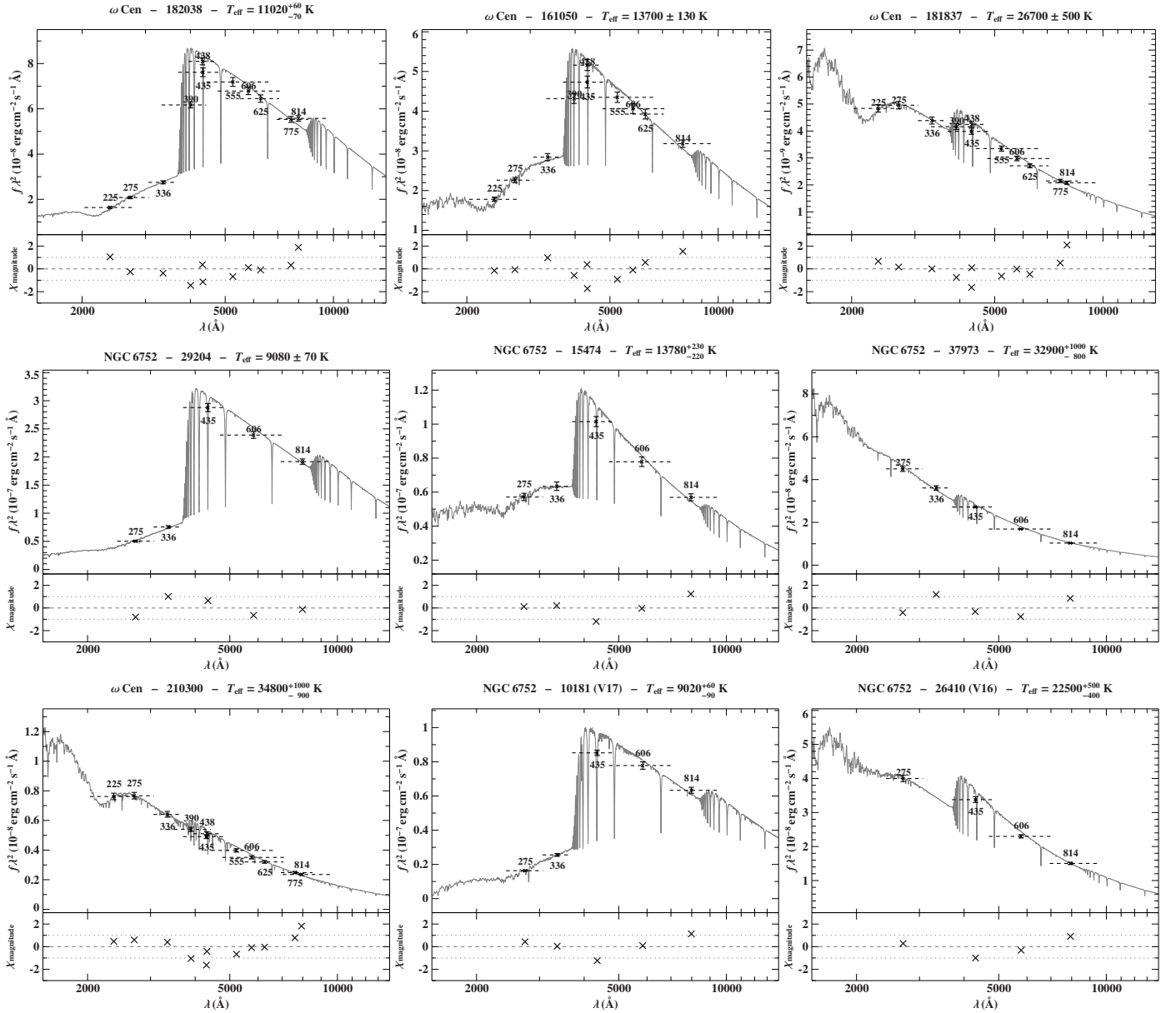


Fig. 6. Examples of photometric (SED) fits with free parameters Θ and T_{eff} . On the y -axis, we plot the flux f_{λ} multiplied by λ^2 . The best-fit model is plotted in grey while the flux corresponding to the observed magnitude in each filter is indicated along with the central wavelength of the filter. The horizontal dashed lines show the wavelength coverage of each filter. The top panels show the best fits for an A-BHB, B-BHB, and EHB type star in ω Cen. The middle panels show fits for counterpart stars in NGC 6752. The bottom panels show fits for a blue-hook star in ω Cen, the BSS V17, and the EHB star V16 in NGC 6752. The uncertainty-weighted residuals ($\chi = (\text{mag}_{\text{model}} - \text{mag}_{\text{observed}}) / \text{uncertainty}$) are plotted at the bottom of each fit. The cluster name, star identification number, and resulting $T_{\text{eff}}^{\text{SED}}$ are indicated for each fit.

via the formulae

$$L = 4\pi R^2 \sigma T_{\text{eff}}^4 \quad \text{and} \quad M = \frac{gR^2}{G}. \quad (1)$$

Because the luminosity and mass have an additional dependence on the effective temperature and surface gravity, respectively, these two parameters bear larger uncertainties than the radius. All uncertainties were propagated using the Monte Carlo method; the resulting best-fit values and their uncertainties are stated as the median with 68% uncertainties throughout this work.

We show in Fig. 6 some examples of SED fits for stars at various temperatures in both clusters. The main feature of the SED for the A-BHB and B-BHB stars is the Balmer jump. This

feature is a good indicator of the stellar effective temperature in BHB stars⁷. The hotter EHB stars have a less prominent Balmer jump and are characterized by an increasing flux at short wavelengths (keeping in mind that the y -axis is the flux multiplied by λ^2). Above 30 kK, the T_{eff} obtained from the SED fits are generally less precise. The dip in the UV flux of the models is due to the 2200 Å bump present in the interstellar extinction curve. This feature is stronger in ω Cen than in NGC 6752 because the reddening of the former is higher.

Metallicities from SED fits. The surface metallicity of BHB stars is difficult to determine from MUSE spectroscopy because

⁷ With magnitudes on both sides of the Balmer jump, the surface gravity can also be estimated from the SED.

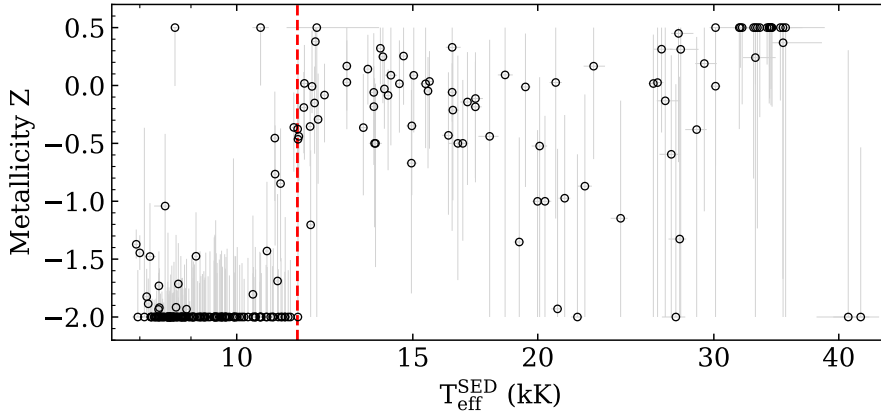


Fig. 7. Metallicity versus effective temperatures obtained from the photometric fits of the stars in ω Cen. The vertical line at 11.5 kK indicates the position of the G-jump.

of the lack of iron-group spectral lines and the low resolution. However, the forest of spectral lines from heavy elements in the near-UV (NUV) and UV regions of the spectra can block a significant amount of flux. Generally speaking, a higher metallicity increases the strength of the metal lines in the UV and consequently suppresses the UV flux, thus affecting the WFC3/UVIS filter at the shortest wavelength ($F225W$ and $F275W$). The flux that is blocked is then emitted at longer wavelengths for a fix T_{eff} . As a test, we performed SED fits of the stars in ω Cen where θ , T_{eff} , and the metallicity Z were left free to vary, while $E(44-55)$ was fixed to 0.12 mag. We used the data in ω Cen to perform this test because the Bellini et al. (2017a) catalog includes magnitudes in the $F225W$ filter. Figure 7 shows the resulting metallicity as a function of T_{eff} . Although Z is not well constrained, the sudden increase in atmospheric metallicity due to the transition from a convective to a radiative atmosphere is clearly visible and happens around 11.5 kK, as expected. For the hotter stars, the metallicities scatter around the solar value ($Z = 0$). This supports our decision to use a solar metallicity in the spectral analysis of the stars hotter than 11.5 kK. This exercise demonstrates that SED fits can be a powerful investigation tool, more so when UV magnitudes are available. In ω Cen, we have ideal conditions to probe the atmospheric metallicity: well-calibrated NUV and UV magnitudes combined with well-constrained distance and reddening for the stars.

4. The final samples

We used spectra with a $S/N \geq 20$ in our analysis. The resulting fit for each star was visually inspected, and those with poor fits in terms of reduced χ^2 and residuals were removed from the sample. Stars that were outliers in some of the derived parameters (e.g., T_{eff} , radius, mass) were also individually inspected. A few additional stars were excluded from the sample after these checks. In most cases, the MUSE spectra were contaminated by the light of a very close-by companion. Even though PAMPELMUSE is efficient at “deblending” the spectra, it is limited, especially for exposures with poor atmospheric conditions and very faint stars. We also found issues when one or more spectra from individual exposures were of especially poor quality, most often due to the star being very close to the edge of the field of view on these particular exposures. With these criteria, we ensure that our final sample contains, to the best of our knowledge, stars for which we have good atmospheric parameters. We note that the radial velocity of all stars in our final sample is consistent with cluster membership. For ω Cen, we also verify their membership via the proper motions of Bellini

et al. (2017a). The final samples contain 302 and 130 HB stars in ω Cen and NGC 6752, respectively. In Sect. 6, we discuss the analysis of five hot BSSs in NGC 6752.

5. Atmospheric parameters

Here, we present the atmospheric parameters derived from our fits of the MUSE spectra. The tabulated results are only available online as Tables B.1 and B.2 (see Appendix B). In Sect. 5.1 we use a color-color plane to identify the location of the HB jumps in terms of their effective temperatures. In Sect. 5.2, we construct the Kiel diagram ($\log g - T_{\text{eff}}$), and in Sect. 5.3 we discuss the variation in helium abundances along the HB. Finally, we compare our results with previous surveys from the literature in Sect. 5.4.

5.1. Color-color plane and the location of the HB jumps

Brown et al. (2016) used a particular combination of HST magnitudes from optical and NUV filters to study the properties of the HB in 53 galactic GCs, including ω Cen. We use the same combination of colors in Fig. 8 to display the stars in our samples. On the y-axis, we use the color index $C_{F275W, F336W, F438W} = (m_{F275W} - m_{F336W}) - (m_{F336W} - m_{F438W})$. The effective temperatures obtained from the spectral fits are color-coded and illustrate the temperature progression along the HB very well. In this particular color-color plane, the G- and M-jumps are visible at $m_{F275W} - m_{F438W} \approx -0.3$ and -1.3 , respectively. For ω Cen, we define the position of the jumps – shown with shaded areas in Fig. 8 – as in Brown et al. (2017). For NGC 6752, we used the same method as in Brown et al. (2016) and we align the stars in our sample with those of ω Cen by applying shifts of +0.15 and -0.01 in the x and y directions, respectively. There is a larger scatter of the stars in the color-color plane of NGC 6752 and the jumps are not as clearly visible as in ω Cen. This is due to the use of the significantly wider ACS/WFC $F435W$ filter instead of the WFC3/UVIS $F438W$ filter, which is why this cluster was not included in the photometric sample of Brown et al. (2016). Most importantly, the $F435W$ filter covers the Balmer jump while the $F438W$ filter does not.

Finally, we computed the mean T_{eff} of the stars found in the shaded area⁸ and indicate the resulting values and standard deviations in Fig. 8. The mean T_{eff} of the stars at the G-jump

⁸ A few more stars than seen in the figure are contributing to the mean T_{eff} at the position of the jumps. This is because the jumps are defined in terms of $F275W - F435(438)W$. Some stars have magnitudes in these two filters but not in $F336W$, and therefore they do not appear on the plots.

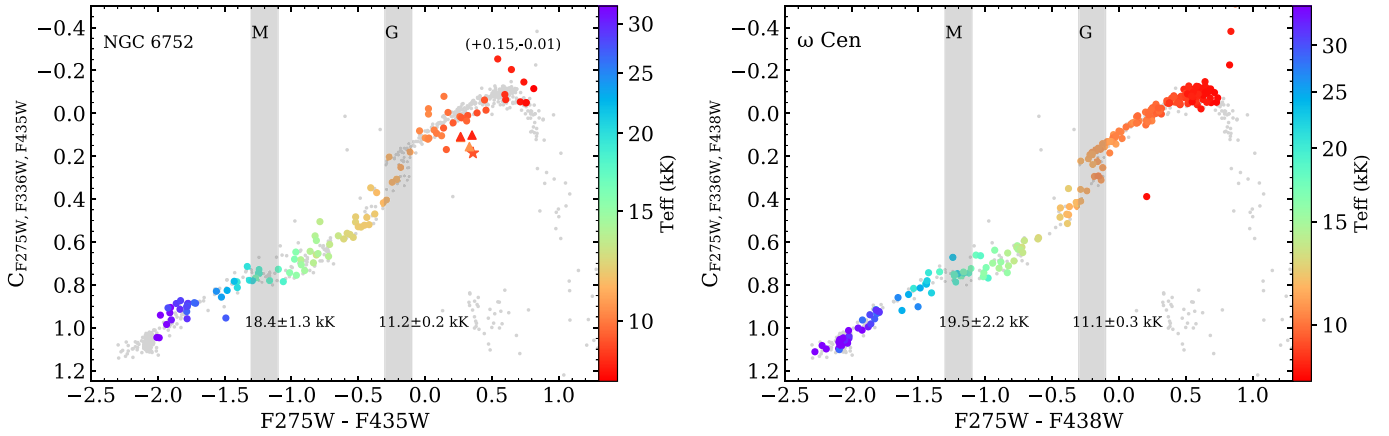


Fig. 8. Color-color plot of the HB stars in our samples. The effective temperatures obtained from the spectral fits are color coded. The positions of the G- and M-jumps are indicated by shaded areas, and we indicate the average temperature and standard deviation of the stars that are included in the areas of the jumps. Three hot BSSs (triangle) and V17 (star) in NGC 6752 are also included. We note that some stars are missing in this plot because they do not have a magnitude in all three filters. For both clusters, we plotted the position of the stars from the photometric catalog of ω Cen as small grey dots. For NGC 6752, we also indicate the shift applied to align the stars with those of ω Cen.

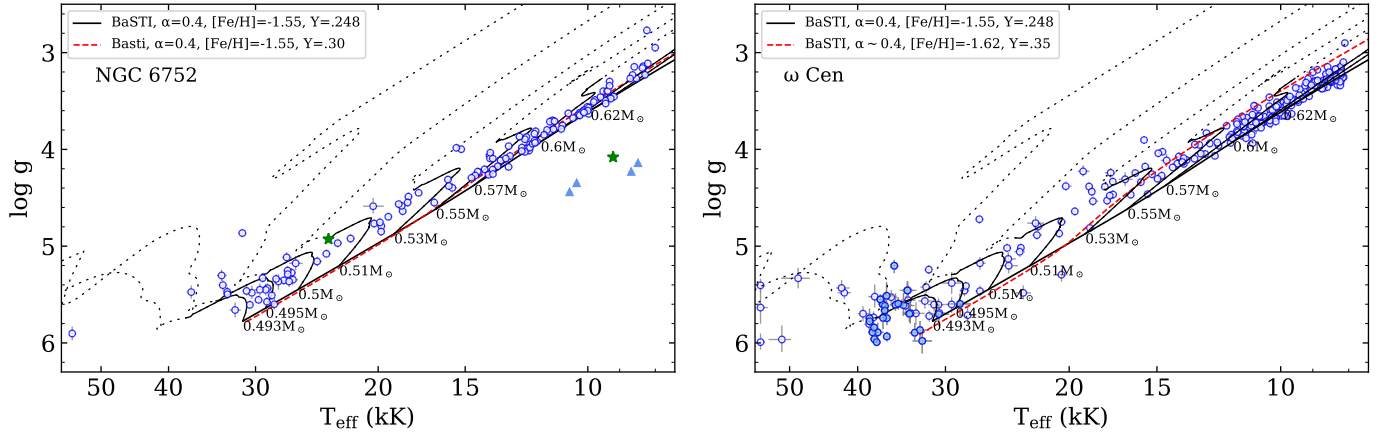


Fig. 9. Kiel diagrams for NGC 6752 (left) and ω Cen (right). We show the theoretical ZAHBs from BaSTI models at a metallicity representative of the clusters and with normal (solid line) and enhanced (red dashed line) helium (Y) abundances. Evolutionary tracks from BaSTI for different masses are also shown with solid lines for the He-core burning phase (i.e., the HB phase) and with dotted lines for the He-shell burning phase (post-HB). The He-rich (blue-hook) objects in ω Cen are indicated with filled symbols. Also shown in NGC 6752 are the two variable stars V16 and V17 (green star symbol), and the four hot BSSs (blue triangles).

in both clusters is in good agreement with the expected value of 11.5 kK. As for the M-jump, we found mean effective temperatures of 18.4 ± 1.3 kK and 19.5 ± 2.2 kK for NGC 6752 and ω Cen, respectively. This is still in reasonable agreement with the theoretical expectations, which are around 20 kK.

5.2. Effective temperature and surface gravity

In Fig. 9, we present the HB stars of our samples in the $T_{\text{eff}}-\log g$ diagram (hereafter Kiel diagram) for each cluster. We also include the position of the theoretical zero-age horizontal branches (ZAHBs) taken from the BaSTI database (Pietrinferni et al. 2021)⁹. Additional (post-)HB evolutionary tracks from BaSTI are also shown for different masses along the HB. The part of the tracks shown with solid lines represents the central He-burning phase, which is also the HB phase. The subsequent post-HB evolution with He-shell burning – which is shorter than the HB phase by a factor of ten – is shown with dotted lines.

For both clusters, we selected theoretical HB models with parameters matching the properties of each cluster. We used the new BaSTI α -enhanced ($\alpha = 0.4$) models (Pietrinferni et al. 2021) with $[\text{Fe}/\text{H}] = -1.55$ ($Z = 0.000886$) and normal helium ($Y = 0.248$). For both clusters, we also show additional theoretical ZAHBs for helium-enhanced models ($Y = 0.30$ for NGC 6752 and $Y = 0.35$ for ω Cen¹⁰).

In both clusters, the cool HB stars ($T_{\text{eff}} \lesssim 14\text{--}15$ kK) sit on the ZAHB as predicted from the helium-normal models. In NGC 6752, the distribution of the cooler HB stars is tightly clustering on the ZAHB. This is expected, because the evolutionary tracks of stars with $M \gtrsim 0.57 M_{\odot}$ evolve towards the asymptotic giant branch almost parallel to the ZAHB. This clustering of the cold stars on the ZAHB is also present in ω Cen, although with a larger scatter. Interestingly, while the A-BHB stars in NGC 6752 form a very narrow sequence in the $F275W-F606W$ CMD (see Fig. 3), the equivalent stars in ω Cen have a larger scatter, which

⁹ <http://basti-iac.oa-teramo.inaf.it/>

¹⁰ We note here that the updated α -enhanced BaSTI models still only include Y up to 0.30, and therefore the $Y = 0.35$ model is from Pietrinferni et al. (2006).

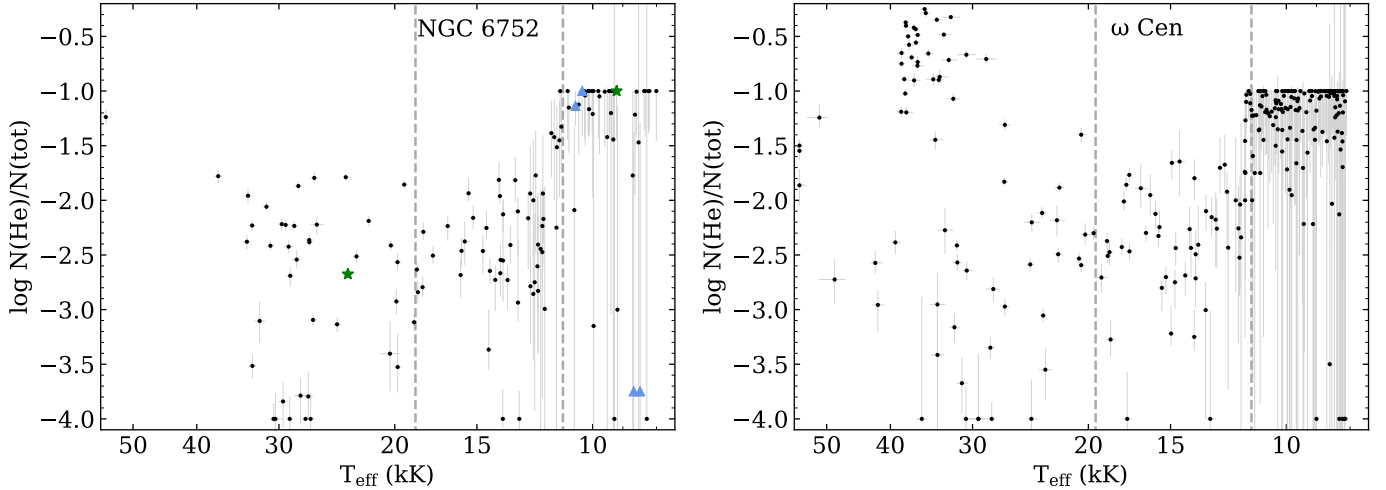


Fig. 10. Helium abundance as a function of T_{eff} . The two vertical lines indicate the positions of the G- and M-jumps at the T_{eff} determined in Fig. 8.

is reminiscent of what is seen in the Kiel diagram. This feature is therefore unlikely to be an artifact coming from our spectral analysis. The scatter could be due to the spread in metallicity among the stars of ω Cen, as the metallicity affects the position of the theoretical ZAHB in the Kiel diagram. In addition, a metallicity spread among the A-BHB stars could also produce some variations in the derived T_{eff} (see Sect. 3.4). It is clear from Fig. 9 that the cool HB stars in ω Cen do not originate from the helium-enriched population; these models predict the stars to have lower surface gravity (i.e., higher luminosity) than what we measure. This is consistent with the findings of Joo & Lee (2013) and Tailo et al. (2016) who used population synthesis of the MS, subgiant, and horizontal branches to reproduce the main features of the CMD of ω Cen, and thus populated most of the cool part of the BHB with metal-poor and helium-normal objects.

For both clusters, we see in Fig. 9 that most of the stars hotter than ~ 15 kK lie above the ZAHB, but still below the terminal-age HB (TAHB; i.e., the end of the He-core burning phase). We do not know the reason behind this shift for the hotter stars, but LeBlanc et al. (2010) showed that elemental stratification in the radiative atmosphere of B-BHB has an effect on the hydrogen line profiles. The authors showed that this could result in underestimation of the $\log g$ derived with homogeneous model atmospheres such as the ones we use for this work.

The few objects found above the TAHB correspond to the evolved post-HB phase where the nuclear burning occurs in a shell. These stars are more luminous and have larger radii than those on the HB; they are also brighter than the bulk of HB stars and are often referred to as UV-bright objects (see e.g., Moehler et al. 2019). In NGC 6752, the low-gravity star (id 15070, $T_{\text{eff}} = 31.3$ kK, $\log g = 4.86$) is much brighter ($F_{275W} = 13.1$) than stars of similar color in the CMD shown in Fig. 3. This object is also known as UIT-1 (from the Ultraviolet Imaging Telescope, Landsman et al. 1996). An independent study found $T_{\text{eff}} = 32 \pm 2$ kK and $\log g = 4.9 \pm 0.2$ dex from an optical HST spectrum (P. Chayer, priv. comm.). Moreover, we find that most of the stars with a post-HB position in the Kiel diagram of both clusters correspond to brighter objects than the bulk of HB stars in the NUV-optical CMD (Fig. 3). In the optical CMD (Fig. 2), they appear shifted to the left compared to the other stars. In NGC 6752, we have identified, for the first time, a hot hydrogen-rich sdO (H-sdO, id 738) with $T_{\text{eff}} \sim 55$ kK that corresponds to the bluest object in the optical CMD of NGC 6752 (Fig. 2).

Finally, the five hot BSSs in NGC 6752, including V17 (see Sect. 6), are significantly below the ZAHB, as expected.

5.3. Helium abundances

The fact that the B-BHB stars, essentially those between the two jumps (Fig. 8), are shifted downward in the color-color plane is explained by an increase in atmospheric metallicity and a decrease in helium abundance, both being the result of diffusion processes as the surface convection vanishes (Brown et al. 2016). Figure 10 shows our results in the T_{eff} -He plane.

As mentioned previously, the He lines in stars colder than the G-jump are very weak and are not necessarily visible in the MUSE spectra. This is reflected in the very large error bars on the helium abundance of the coldest stars, meaning that it is poorly constrained. Nevertheless, the spectral fit for the majority of stars colder than the G-jump is consistent with a solar helium abundance. Figure 10 shows the expected decrease in He abundance in the stars hotter than the G-jump (indicated with a dashed line) until ~ 15 kK. In stars hotter than 15 kK, the He values scatter mostly between -2 dex and -3 dex. In ω Cen, Fig. 10 clearly shows that our sample includes a handful of He-rich stars with T_{eff} between 30 and 40 kK. As expected, we did not find any such objects in NGC 6752. This is one of the differences between the HB morphology of the two clusters. These He-rich stars form the blue-hook population of ω Cen that is located at the faint end of the HB in the optical CMD of Fig. 2. In the F_{275W} - F_{606W} CMD of ω Cen (Fig. 3), the end of the HB appears to be split into two narrow vertical strips. The He-rich blue-hook stars in our sample are all found to lie on the bluest strip. With the MUSE spectra, we did not aim to derive accurate individual He abundances. However, taken globally, our results are in good agreement with the previous spectroscopic analyses in NGC 6752 (Moehler et al. 2000; Moni Bidin et al. 2007) and ω Cen (Moehler et al. 2011; Moni Bidin et al. 2012; Latour et al. 2018).

5.4. Comparison with literature results

In terms of the stellar parameters derived from optical spectra, Moni Bidin et al. (2012) found that the surface gravity of the HB stars colder than ~ 18 kK in ω Cen was systematically lower than the canonical ZAHB and lower than the $\log g$ of their counterparts in three other clusters studied by the same group. This

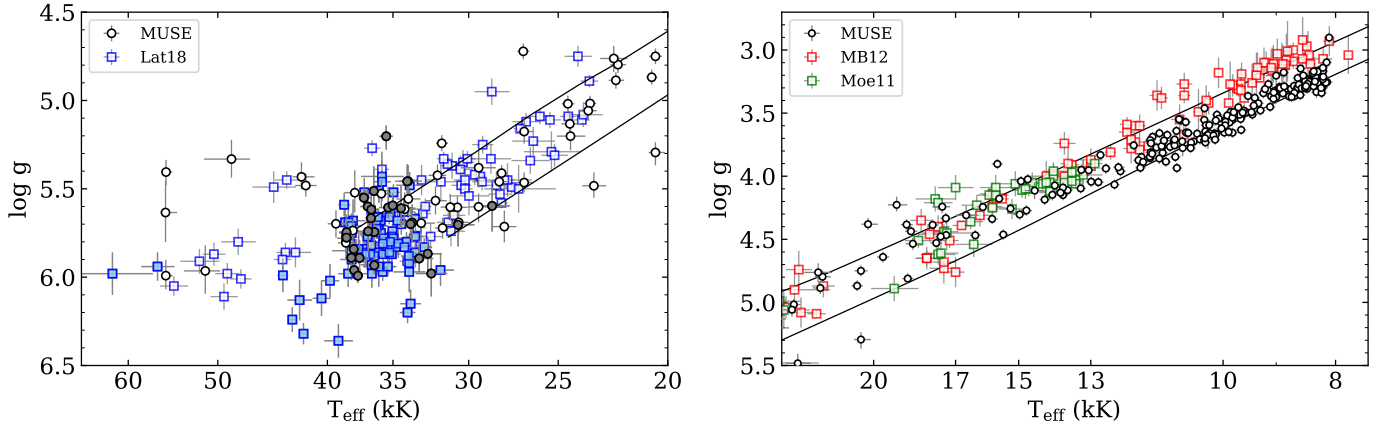


Fig. 11. Kiel diagrams showing the position of the stars in ω Cen for our MUSE sample (black circles) and for samples taken from the literature. Left panel for the EHB stars (blue squares, [Latour et al. 2018](#)) and right panel for the BHB stars (red squares, [Moni Bidin et al. 2012](#), green squares [Moehler et al. 2011](#)). Filled symbols in the left panel indicate the He-rich blue-hook stars. The theoretical HB band for the BaSTI He-normal models is also shown.

is shown in the right panel of Fig. 11 where the [Moni Bidin et al. \(2012\)](#) stars lie on the TAHB while our MUSE stars are on the ZAHB. Interestingly, the B-BHB stars with $T_{\text{eff}} \gtrsim 13$ kK lie above the ZAHB in our analysis as well as in the literature samples ([Moni Bidin et al. 2012](#); [Moehler et al. 2011](#)). This leads us to wonder whether or not it could be a real feature caused by stratification in the atmosphere ([LeBlanc et al. 2010](#)) given that the literature analyses were also performed with chemically homogeneous model atmospheres. For the hot stars in ω Cen, we compare our results with the EHB sample of [Latour et al. \(2018\)](#). We notice that the stars scatter similarly across the EHB in both studies. The He-rich blue-hook stars are more tightly grouped at the end of the EHB at T_{eff} close to 35 kK in the [Latour et al. \(2018\)](#) sample than in our MUSE sample. Taking into consideration that the typical S/N of our blue-hook spectra (see, e.g., star 210300 in Fig. 4) is rather low, we find our results to be very reasonable. The sample of [Latour et al. \(2018\)](#) also includes some very He-enriched stars at higher temperatures and surface gravities than the bulk of the blue-hook objects. Our sample does not include such objects. This does not mean that they are not present in the core of ω Cen, but their absence is most likely attributable to the fact that we are not sampling the faintest part of the blue hook (see Fig. 2) because of the S/N limit.

Figure 12 shows an equivalent comparison to Fig. 11 but for NGC 6752, including the two literature studies available for this cluster ([Moehler et al. 1999](#); [Moni Bidin et al. 2007](#)). This time, the sample of [Moni Bidin et al. \(2007\)](#) closely follows the ZAHB over almost the full T_{eff} range. The slightly lower $\log g$ for stars with $T_{\text{eff}} \gtrsim 15$ kK discussed in Sect. 5.2 is similarly seen in the sample of [Moehler et al. \(1999\)](#). When looking at the comparisons in Figs. 11 and 12, we understand why [Moni Bidin et al. \(2012\)](#) were puzzled by their results in ω Cen. We believe that there are some issues with their analysis of the (cold) stars in ω Cen, but it is unclear what causes the difference.

6. Variable stars and hot blue stragglers in NGC 6752

We looked for variable HB stars that could have been observed by MUSE in our two clusters. We found only two such variable stars, both in NGC 6752. The two stars are among the HB variables identified by [Momany et al. \(2020\)](#), who refer to them as vEHB-1 and vEHB-3. However, these two stars were already

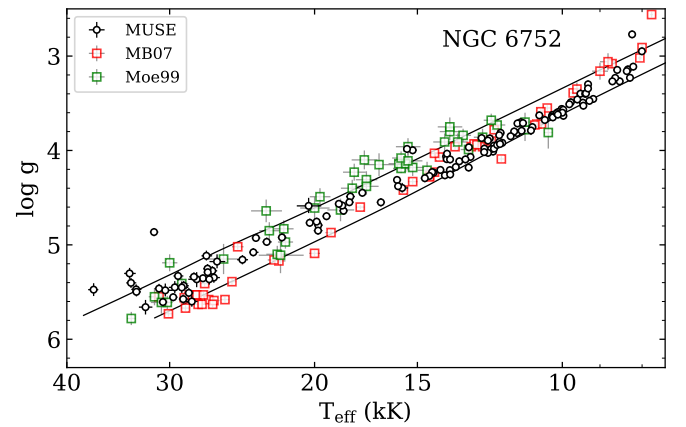


Fig. 12. Kiel diagram showing the position of the stars in NGC 6752 for our MUSE sample (black circle) and for samples taken from the literature ([Moni Bidin et al. 2007](#), red squares and [Moehler et al. 1999](#), green squares).

known as V16 and V17 in the variable star catalog of [Kaluzny & Thompson \(2009\)](#)¹¹. According to the literature, the periods of V16 and V17 are ~ 19.5 and 3.2 days, respectively. We indicate the position of the two variables with green star markers in the CMD (Fig. 2) and atmospheric parameters diagrams (Figs. 9–10). V16 is located directly on the EHB in the CMD and has $T_{\text{eff}} = 23.6$ kK and $\log g = 4.9$. Its spectrum and best fit are shown in Fig. 5. With these parameters, the star blends in with the other EHB stars in the $\log g - T_{\text{eff}}$ and He- T_{eff} planes. Its spectrum does not show any conspicuous features, and appears similar to that of other stars with similar parameters (see also Fig. 5).

V17 sits among a conspicuous small group of six objects located in between the blue straggler region and the HB (see Fig. 2). The atmospheric parameters obtained for V17 ($T_{\text{eff}} = 9200$ K, $\log g = 4.08$) confirm that the star does not belong to the HB; it lies below the ZAHB (see Fig. 9). Our best fit of V17 is shown in Fig. 13. This star is also among the sample of BSSs studied with high-resolution spectroscopy by [Lovisi et al. \(2013\)](#). The authors derived $T_{\text{eff}} = 9016$ K and $\log g = 4.1$ from

¹¹ In the following, we adopt the nomenclature of [Kaluzny & Thompson \(2009\)](#).

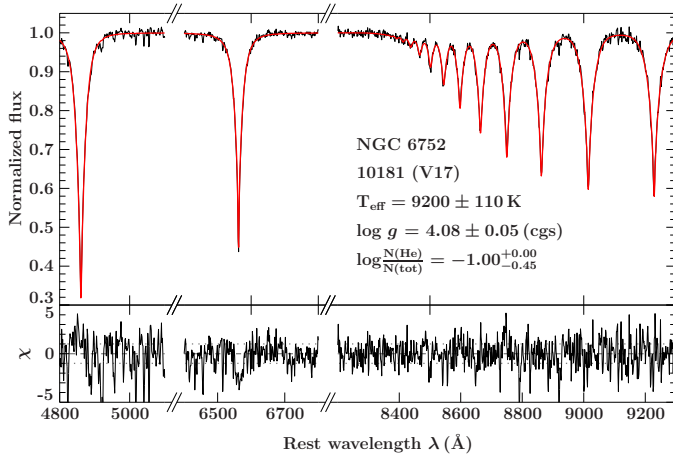


Fig. 13. Best fit of the spectrum of the variable BSS V17 in NGC 6752. The top panel shows the best fit (red) to the normalized spectrum (black). The lower panel displays the residuals. Only the regions with spectral lines of hydrogen are shown.

comparison with isochrones¹². In the sample of these latter authors, there are two additional BSSs located in the same region of the CMD as V17. The authors found that these three objects, being the three hottest of their sample, have higher iron abundances than the cluster value of $[\text{Fe}/\text{H}] = -1.5$. The authors interpreted this in terms of radiative levitation affecting the chemistry of the hot BSSs. From the BSSs studied in a few other GCs by the authors, the onset of radiative levitation, indicated by an increase in Fe abundance but also a decrease in oxygen, starts at $T_{\text{eff}} \sim 7800$ K (Lovisi et al. 2013). Among the small group of hot and bright BSSs in the CMD of NGC 6752, four additional stars were observed by MUSE (triangles in Fig. 2). We retrieved their spectra and fitted them in the same way as the other stars of our sample. As seen in Fig. 9, all of them lie below the HB and we obtained effective temperatures of between 8400 K and 10 600 K. Because they are affected by diffusion, we fitted the stars with the $Z = 0.0$ model grid.

Momany et al. (2020) argue that the variability they observed (typically over periods of 2–10 days and with $\Delta U \sim 0.05$ –0.2 mag) in a subset of EHB stars in three GCs, including V16 and V17, is caused by magnetic spots present at the surface of the stars. The (weak) magnetic fields would be generated by the He II convective zone as it reaches the surface in the atmosphere of EHB stars with T_{eff} close to that of the M-jump. While V16 is a genuine EHB star with $T_{\text{eff}} = 23$ kK, V17 is a different type of object. It is a hot BSS that is significantly colder than the other EHB variables. It is not clear whether the same mechanism can also produce such variability in a BSS. We note that while some BSSs are known to be in binary systems (Giesers et al. 2019), V17 does not show RV variations and its variability cannot be explained by the presence of a close companion (Momany et al. 2020).

7. Mass, radius, and luminosity

The mass of an HB star is tightly correlated with its effective temperature. The mass of the hottest EHB stars, as well as the blue-hook objects, is essentially that of their He-core, because their very light hydrogen envelope ($M \lesssim 0.01 M_{\odot}$) makes a

negligible contribution. There is only a small range of possible masses for the He-core (~ 0.45 – $0.50 M_{\odot}$) dictated by the mass required for the He-flash (Dorman et al. 1993). Therefore, the HB forms a sequence of increasing stellar mass as the hydrogen envelope becomes “thicker” with decreasing effective temperature.

For EHB stars in the Galactic field, mass determinations using various methods, including asteroseismology and eclipsing binaries, are in line with theoretical expectations (see, e.g., Fontaine et al. 2012; Schaffenroth et al. 2022; Schneider 2022). The situation is different in GCs, especially for the two clusters involved in our study. In NGC 6752, Moni Bidin et al. (2007) reported groups of stars with anomalously low or high masses along the HB, with the peculiarity that all BHB stars colder than 10 kK have anomalously low masses. A similar issue was also reported in ω Cen; Moni Bidin et al. (2011) derived masses lower than the canonical values for the BHB and EHB stars. Similarly, low masses were reported by Moehler et al. (2011) for stars colder than 20 kK and by Latour et al. (2018) for the EHB and blue-hook stars. A mass distribution for BHB or EHB stars peaking around $0.35 M_{\odot}$ is difficult to reconcile with evolutionary models. Although various methods were used to derive stellar masses in these previous studies, the results were never fully consistent with theoretical predictions. Here, we attempt to reconcile spectroscopic masses with evolutionary prescriptions by combining the latest state-of-the-art data and methods – as described in Sect. 3.5 – to ultimately derive masses.

In Fig. 14 we show the radii, luminosities, and masses of the stars in both clusters as a function of the effective temperatures obtained from the photometric fits ($T_{\text{eff}}^{\text{SED}}$). The results are available in the online Tables B.3 and B.4 (see also Appendix B). The theoretical predictions from the ZAHB and TAHB models with normal and enhanced helium abundances are indicated as well.

In both clusters, the stars closely follow the theoretical T_{eff} –radius relation of the ZAHB. The agreement between our derived luminosity and the predictions is also very good in both clusters for stars up to ~ 18 kK. Beyond that temperature, the scatter increases for the stars in NGC 6752, but the position of the stars remains consistent with the theoretical HB. In ω Cen, there is a significant fraction of “underluminous” stars in this hot regime. However, we note that the underluminous objects are also the stars with radii smaller than the theoretical ZAHB prediction. In NGC 6752, the stellar masses follow the expected decreasing trend with T_{eff} , but are systematically lower (by $\sim 0.05 M_{\odot}$) than the theoretical prediction up to ~ 18 kK, where the masses are then in better agreement with the models. Typical uncertainties on the masses are of $\pm 0.15 M_{\odot}$, which is considerably larger than the systematic difference observed. The behavior is similar in ω Cen, but with a large scatter in the masses of the cool stars compared to NGC 6752. This is related to the larger scatter seen in $\log g$ in the Kiel diagram. As for the hottest stars ($T_{\text{eff}} \gtrsim 30$ kK), they also have lower masses than expected. This is especially obvious in the case of the He-rich (blue-hook) stars in ω Cen.

We also fitted the SEDs of the stars with T_{eff} fixed to the spectroscopic values (see Fig. A.3). This has little effect on the results for the cooler stars where $T_{\text{eff}}^{\text{SED}}$ and $T_{\text{eff}}^{\text{spectro}}$ are in good agreement. For the hotter stars, it does not lead to better agreement between observations and theoretical models. In particular, the masses remain lower than expected, and this is the case for the whole temperature range. We discuss these results in more detail in Appendix A.

For both clusters, in addition to the HB tracks for He-normal ($Y = 0.248$) models, we also show the tracks for He-enriched

¹² They identify it as BSS10.

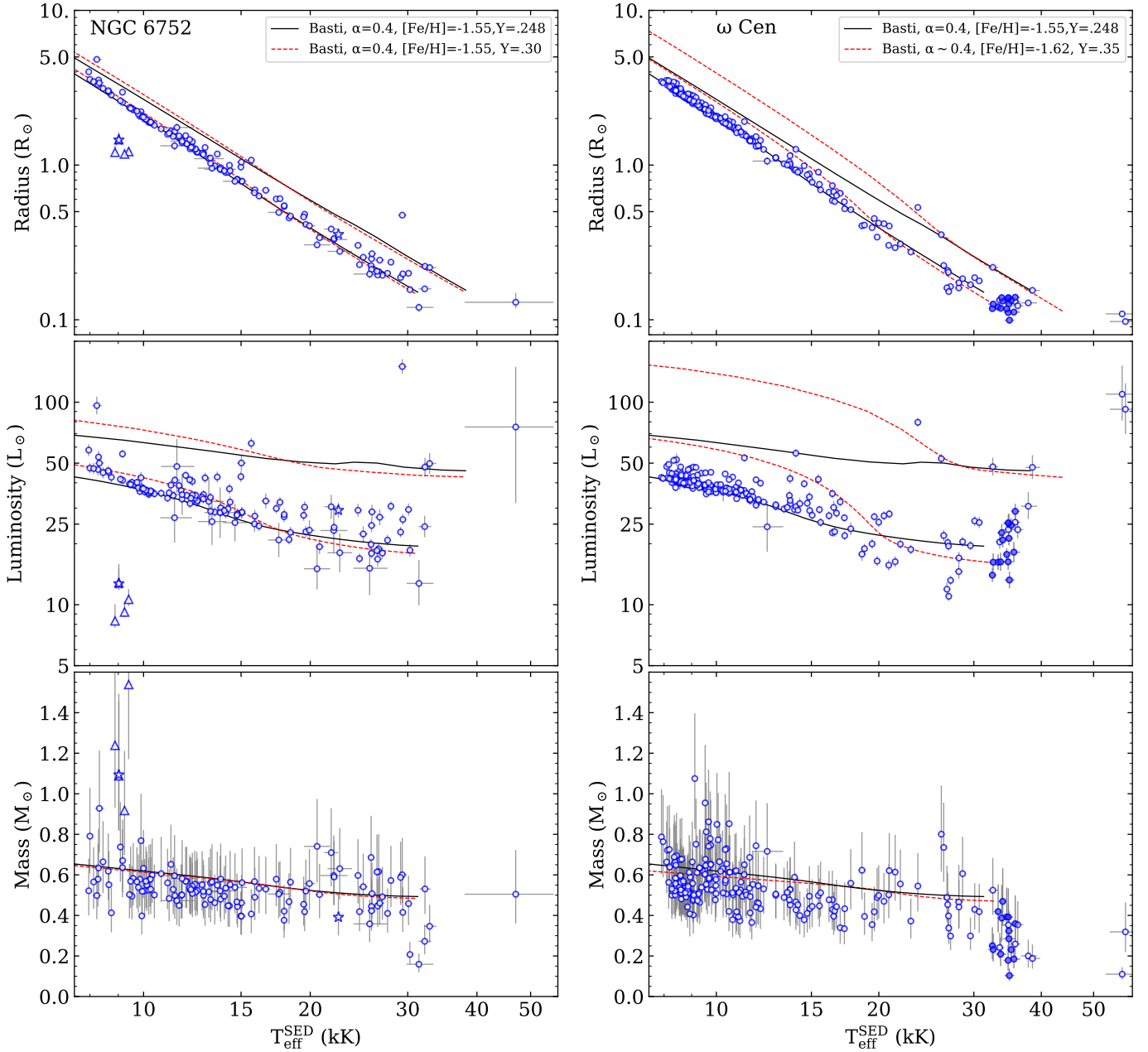


Fig. 14. Radius, luminosity, and mass versus T_{eff} for the stars in NGC 6752 (left panels) and ω Cen (right panels). T_{eff} here is obtained from the SED fit. The two variables (asterisks) and three BSSs (triangles) in NGC 6752 are marked. The filled symbols in ω Cen indicate the He-rich (blue-hook) stars. We show the theoretical ZAHB and TAHB for He-normal (solid) and He-enriched (dashed) models.

models. While the He-enriched population in ω Cen is believed to have a helium content of as high as $Y = 0.35$ – 0.4 (Norris 2004; King et al. 2012), that of NGC 6752 would have, at most, $Y = 0.3$ (Milone et al. 2018; Martins et al. 2021). In the latter case, the small difference in helium content does not significantly affect the position of the HB tracks. However, the models with $Y = 0.35$ (shown for ω Cen) predict larger and more luminous stars than what we derived for the stars with T_{eff} below ~ 20 kK. At higher T_{eff} , the He-normal and He-enriched tracks predict similar properties. As concluded from the Kiel diagram, we can conclude that the cold HB stars in ω Cen originate from a He-rich subpopulation with $Y \gtrsim 0.35$. This is consistent with the conclusions from the population synthesis analysis of Tailo et al. (2016), who populated the colder part of the HB with helium-normal stars. However, these authors populate everything hotter

than ~ 13 kK with stars having increasingly more helium, from $Y = 0.30$ to $Y = 0.37$, and they populate the blue hook with model stars having $Y = 0.37$. Unfortunately, it is in the hottest part of the HB that the He-enriched models show the smallest difference from the helium-normal models.

In the course of our SED fits in ω Cen, we realized that two stars (id 240693, 142667) appear to be hotter than estimated from the spectroscopic fits (T_{eff} between 50 and 55 kK). We fitted the photometry of these objects with a grid of DA white dwarf models (Reindl et al. 2016) and estimated $T_{\text{eff}} \sim 110$ kK and 75 kK, respectively, for these two hot stars¹³. With such high temperatures, these stars are possibly in a post-AGB phase.

¹³ They are outside the range plotted in Fig. 14.

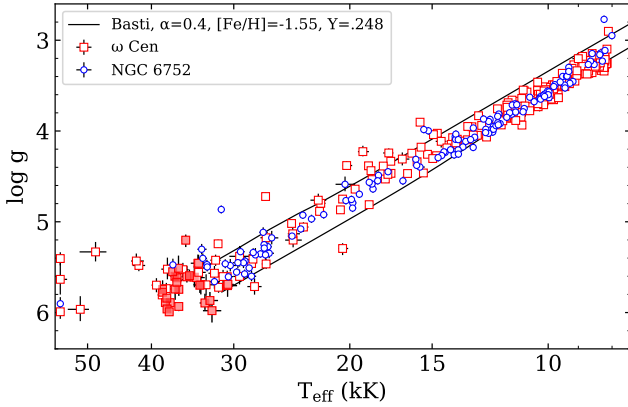


Fig. 15. Kiel diagram showing the position of the stars in NGC 6752 (circle) and ω Cen (square). The He-rich (blue-hook) objects are indicated with filled symbols.

We also fitted the SEDs of the five BSSs in NGC 6752. As expected, these stars are smaller and less luminous than the He-core burning HB. We note that the range of T_{eff} obtained from the SED fits of the BSSs stars is restricted to 8800–9400 K. We find masses of between 0.9 and 1.5 M_{\odot} , for these five objects, which is within the expected values for BSSs in old GCs (De Marco et al. 2005).

8. Comparison between both clusters

Although they have a similar HB morphology, ω Cen and NGC 6752 are fundamentally different as GCs. The former is the most complex cluster in the Milky Way and is believed to be the nuclear star cluster of a dwarf galaxy accreted by the Milky Way or the result of the merger of two or more clusters (see, e.g., Bekki & Freeman 2003; Ibata et al. 2019; Pfeffer et al. 2021). Its stars have a metallicity spread of more than one order of magnitude ($-2.2 \lesssim [\text{Fe}/\text{H}] \lesssim -0.6$, Johnson & Pilachowski 2010) and a significant spread in helium abundance ($\delta Y \approx 0.1\text{--}0.15$) as well (Norris 2004; King et al. 2012). On the other hand, NGC 6752 is a relatively simple GC, essentially mono-metallic (Carretta et al. 2009a) with a modest spread in helium abundance of $\delta Y \lesssim 0.04$ (Milone et al. 2018) and showing a Na-O anticorrelation typical of Milky Way GCs (Carretta et al. 2009b).

Given these fundamental differences between the two GCs, we thought it worthwhile to compare the properties of their HB stars in the Kiel diagram (Fig. 15) and in terms of radius, luminosity, and mass (Fig. 16). We do not see any significant difference in the position of the stars in the Kiel diagram between NGC 6752 and ω Cen besides the absence of He-rich (blue-hook) stars in NGC 6752. This is different from the conclusion of Moni Bidin et al. (2011, 2012), who found differences in $\log g$ and mass between the HB stars of ω Cen and those of three other clusters (namely NGC 6752, M80, and NGC 5986). Prabhu et al. (2022) also reported differences in magnitude (in the UV-optical CMD), radius, and luminosity between the HB stars in ω Cen and those in M13. These latter authors found the hot HB stars in ω Cen to be fainter than model predictions by ~ 0.5 mag in the far-UV (FUV). According to their study, these same stars also appear to have smaller radii and lower luminosity than their counterparts in M13. The comparison between the radius, luminosity, and mass (see Fig. 16) obtained for the stars in our two samples does not suggest any fundamental difference in these parameters between the HB stars in ω Cen and NGC 6752. We mention in Sect. 5 that the cold stars in ω Cen show greater scatter than

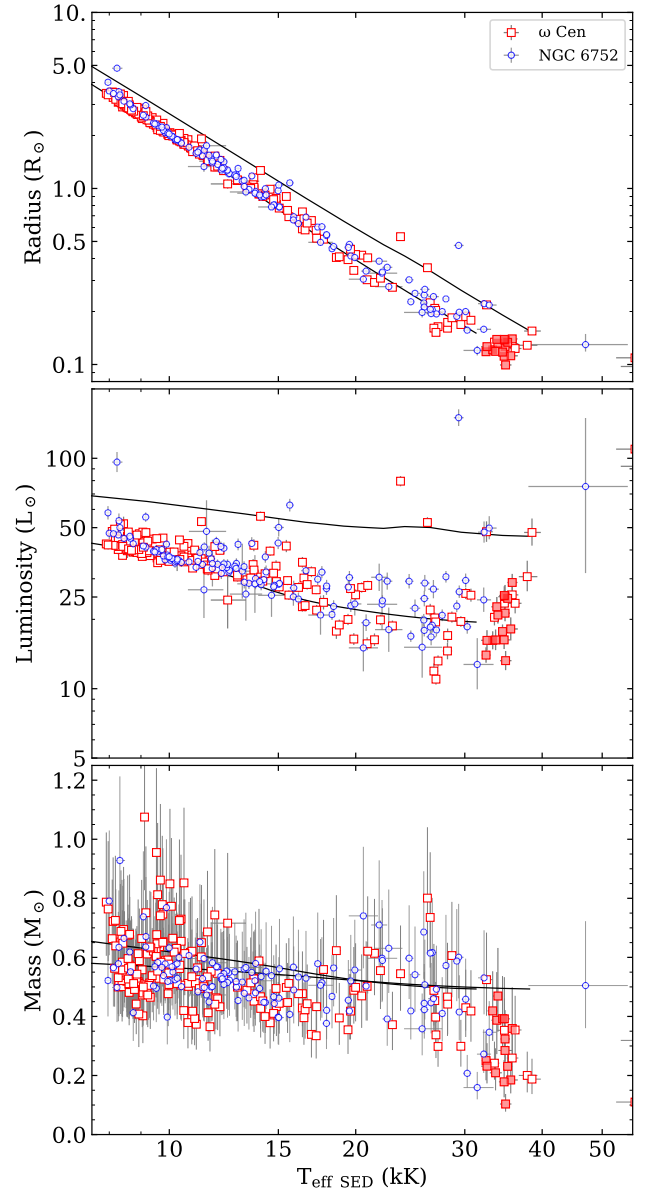


Fig. 16. Same as Fig. 14 but comparing the results for NGC 6752 (circle) and ω Cen (square).

those of NGC 6752 in the Kiel diagram. This is also the case in the radius, luminosity, and mass plots. As mentioned above, this behavior might be linked to the metallicity spread in ω Cen.

The remaining major difference between the HB morphology of both clusters is related to the He-rich blue-hook stars, which are present in ω Cen but absent in NGC 6752. Only a few Galactic GCs have a sizable population of blue-hook stars. Their presence appears to be related to cluster mass, meaning that blue-hook populations are only found in massive clusters (Moehler et al. 2004; Rosenberg et al. 2004; Dieball et al. 2009; Brown et al. 2010; Johnson et al. 2017). However, the presence of a stellar population with large He enhancement ($\delta Y \gtrsim 0.09$, Milone et al. 2018) also seems to favor the formation of blue-hook stars¹⁴. The recent characterization of NGC 6402

¹⁴ M54, the nuclear star cluster of the Sagittarius Dwarf Galaxy, is an apparent exception as it does not show a particularly high He enhancement (Milone et al. 2018) but has a large population of blue-hook stars (Brown et al. 2016).

supports this idea (D’Antona et al. 2022). As for NGC 6752, it is not massive enough and does not have a sufficiently He-enriched population to produce blue-hook stars.

9. Summary

We analyzed the MUSE spectra of more than 400 HB stars hotter than 8 000 K found in the central regions of the GCs ω Cen and NGC 6752. The MUSE spectra cover the 4750–9350 Å spectral range and include H_α , H_β , the Paschen series, He II $\lambda 5412$, and a handful of He I lines depending on the spectral type. We fitted these spectral features with dedicated grids of hybrid LTE/NLTE model atmospheres in order to derive T_{eff} , $\log g$, and helium abundance. We also used our model atmospheres to fit the HST photometry of the stars in our samples, that is, in up to 5 (for NGC 6752) and 11 (for ω Cen) filters. We used the SED of the stars colder than 13 kK to estimate the average reddening of the clusters. We obtained values in perfect agreement with the literature. From the SED fits of the stars in our sample, we derive radii, luminosities, and masses by making use of the known distances of the clusters.

When plotted in the $\log g - T_{\text{eff}}$ diagram, the positions of the stars colder than ~ 15 kK in both clusters are in excellent agreement with theoretical α -enhanced BaSTI ZAHB models with normal helium abundance ($Y = 0.247$) and a metallicity representative of the mean metallicity of the clusters (i.e., $[\text{Fe}/\text{H}] = -1.55$). In ω Cen, the position of these colder stars ($T_{\text{eff}} \lesssim 15$ kK) in the Kiel diagram excludes the possibility that they come from the He-rich ($Y = 0.35$) subpopulation of the cluster. Their luminosities and radii also support this conclusion. A milder He-enrichment (e.g., $Y = 0.3$) does not produce measurable differences in terms of $\log g$ and radius, and only a slightly higher luminosity in stars colder than 15 kK. We therefore cannot exclude the possibility that some of the BHB stars have a modest He enrichment.

We detect the onset of atmospheric diffusion that separates the A-BHB from the B-BHB stars using three different indicators: via the T_{eff} of the stars at the position of the G-jump in the color-color plane (Fig. 8), via the sharp drop in helium abundance measured from the MUSE spectra (Fig. 10), and via the increase in atmospheric metallicity measured from the photometric fits of the stars in ω Cen (Fig. 7). All of these diagnostics indicate that the transition happens between 11 and 11.5 kK in both clusters.

We estimated the effective temperatures of the stars also as part of the SED fits. The spectroscopic and photometric T_{eff} are in good agreement for stars colder than 15 kK (see Fig. A.2). For the stars hotter than 15 kK, the spectral fits generally return a higher temperature than the photometric fits. This discrepancy between $T_{\text{eff}}^{\text{spectro}}$ and $T_{\text{eff}}^{\text{SED}}$ also affects the reddening that is estimated from the SED when fixing T_{eff} to its spectroscopic value: the hot stars require a larger reddening in order to reproduce the photometric measurements (see Fig. A.1). This is because lowering T_{eff} or increasing $E(B - V)$ has a similar effect on the shape of the SED. For now, it remains unclear as to where this discrepancy in T_{eff} (and reddening) for the hot stars comes from, and whether or not it can be solved is uncertain. Concerning the masses of the HB stars, we find them to be systematically lower than theoretical expectations by about $0.05 M_\odot$ for the HB stars colder than ~ 18 kK. However, this difference is well within the typical uncertainty of $\pm 0.15 M_\odot$ on the individual masses. As for the masses of the EHB stars ($T_{\text{eff}} > 20$ kK), they are significantly influenced by the adopted temperature, either

$T_{\text{eff}}^{\text{SED}}$ or $T_{\text{eff}}^{\text{spectro}}$. The former leads to better agreement with the theory. However, in both cases, the blue-hook stars in ω Cen have significantly lower masses than expected.

We analyzed two of the periodic variables in NGC 6752, namely V16 and V17 (Kaluzny & Thompson 2009). These stars were also presented among the sample of 22 periodic EHB stars discovered in NGC 6752, ω Cen, and NGC 2808 by Momany et al. (2020). We show that, while V16 is a genuine EHB star with $T_{\text{eff}} = 23$ kK, V17 is a hot blue straggler star with $T_{\text{eff}} \sim 9000$ K, which is significantly colder than the other EHB variables discovered by Momany et al. (2020). It is not clear whether or not the mechanism invoked by Momany et al. (2020), that is magnetic fields produced by the presence of surface or subsurface convective layers, can also produce such variability in a BSS. The hot BSSs are clearly too cold for the He II convection zone to reach the surface, but could instead have the He I convection zone close to their surface. If a similar mechanism is indeed responsible for the periodic variations in EHB and in V17, other hot BSSs in GCs might show similar luminosity variations.

10. Conclusion and outlook

In conclusion, we carried out a pioneering spectroscopic and photometric investigation of the population of HB stars in the core of NGC 6752 and ω Cen. Thanks to MUSE, we obtain a first glimpse into the BHB and EHB stars in the center of these two clusters. We find a rich variety of spectral types closely resembling those studied in the outskirts of the clusters. Our spectroscopic analysis demonstrates that the MUSE spectra, in spite of their “red” wavelength coverage, are well suited for the study of blue HB stars in GCs. These spectra, combined with the HST photometry of the stars, allowed us to derive the usual spectroscopic parameters (T_{eff} , $\log g$, helium abundance) but also stellar parameters (radius, luminosity, and mass), which we then compared with theoretical evolutionary models. The analysis method provided us with precise measurements that closely follow the theoretical predictions for radii, luminosities, and position in the Kiel diagram for stars with $T_{\text{eff}} \lesssim 15$ kK. Although some discrepancies between theoretical expectations and observations arise for hotter stars, our results are comparable to those of previous studies.

The numerous observations taken as part of the MUSE GC Survey provide an unprecedentedly large number of homogeneous spectra of HB stars, not only in ω Cen and NGC 6752, but also in other GCs with a blue HB, such as NGC 2808, NGC 1851, NGC 5904, NGC 6656, NGC 6093, and NGC 7078. This creates an opportunity for future detailed studies of several other GCs. The only limitation is the faintness of the EHB stars, but the A-BHB and B-BHB stars are bright enough to have good S/N spectra. Because the MUSE observations are targeting the core regions of GCs, the stars observed also have HST photometry in the five filters included in the HUGS survey (Nardiello et al. 2018; Piotto et al. 2015), providing a reliable dataset to perform SED fits. We also want to include additional FUV and NUV magnitudes from UVIT/AstroSat (Sahu et al. 2022) and STIS/HST (e.g., for NGC 2808, Brown et al. 2001). This will hopefully provide further constraints for the photometric fits, especially for the hot EHB stars. In future papers, we want to analyze the spectra of HB stars in the GCs listed above, but also from additional MUSE observations of ω Cen (Nitschai et al. 2023). These new observations fill most of the spatial gap between the data presented here and the surveys from the literature (see Fig. 1), and include a few stars in common with the

previous studies, allowing us to directly compare the spectroscopic parameters derived from MUSE and other spectra with a bluer spectral range.

In the future, Blue-MUSE (Richard et al. 2019), with a planned spectral coverage of 3500–6000 Å, a resolution of $R \sim 4000$, and a 2 arcmin² field of view, will be a perfect instrument for studying the HB and especially EHB stars in GCs. The wavelength range and resolution will provide spectra similar to those of the FORS2 instrument – which has been used for most literature studies of EHB stars in GCs – but with all the advantages of an IFU.

Acknowledgements. We are most grateful to Andreas Irrgang for the development of the spectrum and SED-fitting tools, his contributions to the model atmosphere grids and his advice to use the isis scripts. We also thank Annalisa Calamida for providing us information about the calibration of HST filters. We acknowledge funding from the Deutsche Forschungsgemeinschaft (grant LA 4383/4-1 and DR 281/35-1) and from the German Ministry for Education and Science (BMBF Verbundforschung) through grants 05A14MGA, 05A17MGA, 05A14BAC, 05A17BAA, and 05A20MGA. S.K. gratefully acknowledges funding from UKRI in the form of a Future Leaders Fellowship (grant no. MR/T022868/1). J.B. acknowledges financial support from the Fundação para a Ciência e a Tecnologia (FCT) through research grants UIDB/04434/2020 and UIDP/04434/2020, national funds PTDC/FIS-AST/4862/2020 and work contract 2020.03379.CEECIND. This research has made use of NASA's Astrophysics Data System Bibliographic Services and the PYTHON packages pandas (Pandas development team 2020; McKinney 2010) and MATPLOTLIB (Hunter 2007).

References

- Adelman, S. J., & Philip, A. G. D. 1996, *MNRAS*, **280**, 285
- Anderson, J., & van der Marel, R. P. 2010, *ApJ*, **710**, 1032
- Anderson, J., Sarajedini, A., Bedin, L. R., et al. 2008, *AJ*, **135**, 2055
- Asplund, M., Grevesse, N., Sauval, A. J., & Scott, P. 2009, *ARA&A*, **47**, 481
- Bacon, R., Accardo, M., Adjali, L., et al. 2010, *SPIE Conf. Ser.*, **7735**, 773508
- Bastian, N., & Lardo, C. 2018, *ARA&A*, **56**, 83
- Baumgardt, H., & Vasiliev, E. 2021, *MNRAS*, **505**, 5957
- Behr, B. B. 2003, *ApJS*, **149**, 67
- Bekki, K., & Freeman, K. C. 2003, *MNRAS*, **346**, L11
- Bellini, A., Anderson, J., Bedin, L. R., et al. 2017a, *ApJ*, **842**, 6
- Bellini, A., Anderson, J., van der Marel, R. P., et al. 2017b, *ApJ*, **842**, 7
- Brown, T. M., Sweigart, A. V., Lanz, T., Landsman, W. B., & Hubeny, I. 2001, *ApJ*, **562**, 368
- Brown, T. M., Sweigart, A. V., Lanz, T., et al. 2010, *ApJ*, **718**, 1332
- Brown, T. M., Cassisi, S., D'Antona, F., et al. 2016, *ApJ*, **822**, 44
- Brown, T. M., Taylor, J. M., Cassisi, S., et al. 2017, *ApJ*, **851**, 118
- Butler, K., & Giddings, J. 1985, Newsletter on the analysis of astronomical spectra, 9 (University of London)
- Caloi, V. 1999, *A&A*, **343**, 904
- Carretta, E., Bragaglia, A., Gratton, R., & Lucatello, S. 2009a, *A&A*, **505**, 139
- Carretta, E., Bragaglia, A., Gratton, R. G., et al. 2009b, *A&A*, **505**, 117
- Catelan, M. 2009, *Ap&SS*, **320**, 261
- Copperwheat, C. M., Morales-Rueda, L., Marsh, T. R., Maxted, P. F. L., & Heber, U. 2011, *MNRAS*, **415**, 1381
- D'Antona, F., Milone, A. P., Johnson, C. I., et al. 2022, *ApJ*, **925**, 192
- D'Cruz, N. L., O'Connell, R. W., Rood, R. T., et al. 2000, *ApJ*, **530**, 352
- De Marco, O., Shara, M. M., Zurek, D., et al. 2005, *ApJ*, **632**, 894
- Dieball, A., Knigge, C., Maccarone, T. J., et al. 2009, *MNRAS*, **394**, L56
- Dorman, B. 1992, *ApJS*, **80**, 701
- Dorman, B., Rood, R. T., & O'Connell, R. W. 1993, *ApJ*, **419**, 596
- Dotter, A., Sarajedini, A., Anderson, J., et al. 2010, *ApJ*, **708**, 698
- Faulkner, J. 1966, *ApJ*, **144**, 978
- Fitzpatrick, E. L., Massa, D., Gordon, K. D., Bohlin, R., & Clayton, G. C. 2019, *ApJ*, **886**, 108
- Fontaine, G., Brassard, P., Charpinet, S., et al. 2012, *A&A*, **539**, A12
- Geier, S., & Heber, U. 2012, *A&A*, **543**, A149
- Giddings, J. R. 1981, PhD thesis, Moscow State University, Russia
- Giesers, B., Kamann, S., Dreizler, S., et al. 2019, *A&A*, **632**, A3
- Gratton, R. G., Bragaglia, A., Carretta, E., et al. 2005, *A&A*, **440**, 901
- Grundahl, F., Catelan, M., Landsman, W. B., Stetson, P. B., & Andersen, M. I. 1999, *ApJ*, **524**, 242
- Hämmerich, S. 2020, Master's thesis, Friedrich-Alexander-Universität Erlangen-Nürnberg, Germany
- Han, Z. 2008, *A&A*, **484**, L31
- Han, Z., Podsiadlowski, P., Maxted, P. F. L., Marsh, T. R., & Ivanova, N. 2002, *MNRAS*, **336**, 449
- Han, Z., Podsiadlowski, P., Maxted, P. F. L., & Marsh, T. R. 2003, *MNRAS*, **341**, 669
- Han, Z., Podsiadlowski, P., & Lynas-Gray, A. E. 2007, *MNRAS*, **380**, 1098
- Harris, W. E. 1996, *AJ*, **112**, 1487
- Heber, U. 2009, *ARA&A*, **47**, 211
- Heber, U. 2016, *PASP*, **128**, 082001
- Heber, U., & Kudritzki, R. P. 1986, *A&A*, **169**, 244
- Heber, U., Kudritzki, R. P., Caloi, V., Castellani, V., & Danziger, J. 1986, *A&A*, **162**, 171
- Heber, U., Irrgang, A., & Schaffenhofer, J. 2018, *Open Astron.*, **27**, 35
- Houck, J. C., & Denicola, L. A. 2000, *ASP Conf. Ser.*, **216**, 591
- Hoyle, F., & Schwarzschild, M. 1955, *ApJS*, **2**, 1
- Hubeny, I., Hummer, D. G., & Lanz, T. 1994, *A&A*, **282**, 151
- Hui-Bon-Hoa, A., LeBlanc, F., & Hauschildt, P. H. 2000, *ApJ*, **535**, L43
- Hummer, D. G., & Mihalas, D. 1988, *ApJ*, **331**, 794
- Hunter, J. D. 2007, *Comput. Sci. Eng.*, **9**, 90
- Husser, T.-O., Wende-von Berg, S., Dreizler, S., et al. 2013, *A&A*, **553**, A6
- Husser, T.-O., Kamann, S., Dreizler, S., et al. 2016, *A&A*, **588**, A148
- Ibata, R. A., Bellazzini, M., Malhan, K., Martin, N., & Bianchini, P. 2019, *Nat. Astron.*, **3**, 667
- Irrgang, A., Przybilla, N., Heber, U., et al. 2014, *A&A*, **565**, A63
- Irrgang, A., Kreuzer, S., & Heber, U. 2018a, *A&A*, **620**, A48
- Irrgang, A., Kreuzer, S., Heber, U., & Brown, W. 2018b, *A&A*, **615**, L5
- Irrgang, A., Geier, S., Heber, U., et al. 2021, *A&A*, **650**, A102
- Irrgang, A., Przybilla, N., & Meynet, G. 2022, *Nat. Astron.*, **6**, 1414
- Johnson, C. I., & Pilachowski, C. A. 2010, *ApJ*, **722**, 1373
- Johnson, C. I., Caldwell, N., Rich, R. M., et al. 2017, *ApJ*, **836**, 168
- Joo, S.-J., & Lee, Y.-W. 2013, *ApJ*, **762**, 36
- Kaluzny, J., & Thompson, I. B. 2009, *Acta Astron.*, **59**, 273
- Kamann, S. 2018, Astrophysics Source Code Library [record ascl:1805.021]
- Kamann, S., Wisotzki, L., & Roth, M. M. 2013, *A&A*, **549**, A71
- Kamann, S., Husser, T. O., Dreizler, S., et al. 2018, *MNRAS*, **473**, 5591
- King, I. R., Bedin, L. R., Cassisi, S., et al. 2012, *AJ*, **144**, 5
- Kinman, T., Castelli, F., Cacciari, C., et al. 2000, *A&A*, **364**, 102
- Kreuzer, S., Irrgang, A., & Heber, U. 2020, *A&A*, **637**, A53
- Kurucz, R. L. 1996, *ASP Conf. Ser.*, **108**, 2
- Landsman, W. B., Sweigart, A. V., Bohlin, R. C., et al. 1996, *ApJ*, **472**, L93
- Latour, M., Randall, S. K., Fontaine, G., et al. 2014, *ApJ*, **795**, 106
- Latour, M., Randall, S. K., Calamida, A., Geier, S., & Moehler, S. 2018, *A&A*, **618**, A15
- LeBlanc, F., Hui-Bon-Hoa, A., & Khalack, V. R. 2010, *MNRAS*, **409**, 1606
- Lisker, T., & Han, Z. 2008, *ApJ*, **680**, 1042
- Lovisi, L., Mucciarelli, A., Dalessandro, E., Ferraro, F. R., & Lanzoni, B. 2013, *ApJ*, **778**, 64
- Marino, A. F., Milone, A. P., Przybilla, N., et al. 2014, *MNRAS*, **437**, 1609
- Martins, F., Chantreau, W., & Charbonnel, C. 2021, *A&A*, **650**, A162
- Maxted, P. F. L., Heber, U., Marsh, T. R., & North, R. C. 2001, *MNRAS*, **326**, 1391
- McKinney, W. 2010, in *Proceedings of the 9th Python in Science Conference*, ed. S. van der Walt & J. Millman, 56
- Michaud, G., Richer, J., & Richard, O. 2011, *A&A*, **529**, A60
- Milone, A. P., Marino, A. F., Renzini, A., et al. 2018, *MNRAS*, **481**, 5098
- Miocchi, P. 2007, *MNRAS*, **381**, 103
- Moehler, S. 2001, *PASP*, **113**, 1162
- Moehler, S. 2010, *Mem. Soc. Astron. Italiana*, **81**, 838
- Moehler, S., Heber, U., & Rupprecht, G. 1997, *A&A*, **319**, 109
- Moehler, S., Sweigart, A. V., Landsman, W. B., Heber, U., & Catelan, M. 1999, *A&A*, **346**, L1
- Moehler, S., Sweigart, A. V., Landsman, W. B., & Heber, U. 2000, *A&A*, **360**, 120
- Moehler, S., Sweigart, A. V., Landsman, W. B., & Dreizler, S. 2002, *A&A*, **395**, 37
- Moehler, S., Sweigart, A. V., Landsman, W. B., Hammer, N. J., & Dreizler, S. 2004, *A&A*, **415**, 313
- Moehler, S., Dreizler, S., Lanz, T., et al. 2007, *A&A*, **475**, L5
- Moehler, S., Dreizler, S., Lanz, T., et al. 2011, *A&A*, **526**, A136
- Moehler, S., Landsman, W. B., Lanz, T., & Miller Bertolami, M. M. 2019, *A&A*, **627**, A34
- Momany, Y., Piotto, G., Recio-Blanco, A., et al. 2002, *ApJ*, **576**, L65
- Momany, Y., Zaggia, S., Montalto, M., et al. 2020, *Nat. Astron.*, **4**, 1092
- Moni Bidin, C. 2018, *Open Astron.*, **27**, 91
- Moni Bidin, C., Moehler, S., Piotto, G., et al. 2006, *A&A*, **451**, 499
- Moni Bidin, C., Moehler, S., Piotto, G., Momany, Y., & Recio-Blanco, A. 2007, *A&A*, **474**, 505
- Moni Bidin, C., Catelan, M., & Altmann, M. 2008, *A&A*, **480**, L1

- Moni Bidin, C., Villanova, S., Piotto, G., Moehler, S., & D’Antona, F. 2011, [ApJ](#), **738**, L10
- Moni Bidin, C., Villanova, S., Piotto, G., et al. 2012, [A&A](#), **547**, A109
- Nardiello, D., Libralato, M., Piotto, G., et al. 2018, [MNRAS](#), **481**, 3382
- Newell, E. B. 1973, [ApJS](#), **26**, 37
- Newell, B., & Graham, J. A. 1976, [ApJ](#), **204**, 804
- Nieva, M. F., & Przybilla, N. 2007, [A&A](#), **467**, 295
- Nitschai, M. S., Neumayer, N., & Clontz, C. 2023, [ApJ](#), submitted
- Norris, J. E. 2004, [ApJ](#), **612**, L25
- Pace, G., Recio-Blanco, A., Piotto, G., & Momany, Y. 2006, [A&A](#), **452**, 493
- Pandas development team 2020, <https://doi.org/10.5281/zenodo.3509134>
- Pelisoli, I., Vos, J., Geier, S., Schaffenroth, V., & Baran, A. S. 2020, [A&A](#), **642**, A180
- Pfeffer, J., Lardo, C., Bastian, N., Saracino, S., & Kamann, S. 2021, [MNRAS](#), **500**, 2514
- Pietrinferni, A., Cassisi, S., Salaris, M., & Castelli, F. 2006, [ApJ](#), **642**, 797
- Pietrinferni, A., Hidalgo, S., Cassisi, S., et al. 2021, [ApJ](#), **908**, 102
- Piotto, G., Milone, A. P., Bedin, L. R., et al. 2015, [AJ](#), **149**, 91
- Prabhu, D. S., Subramaniam, A., Sahu, S., et al. 2022, [ApJ](#), **939**, L20
- Przybilla, N. 2005, [A&A](#), **443**, 293
- Przybilla, N., & Butler, K. 2004, [ApJ](#), **609**, 1181
- Przybilla, N., Butler, K., Becker, S. R., & Kudritzki, R. P. 2006, [A&A](#), **445**, 1099
- Przybilla, N., Nieva, M.-F., & Butler, K. 2011, [J. Phys. Conf. Ser.](#), **328**, 012015
- Quievvy, D., Charbonneau, P., Michaud, G., & Richer, J. 2009, [A&A](#), **500**, 1163
- Recio-Blanco, A., Aparicio, A., Piotto, G., de Angeli, F., & Djorgovski, S. G. 2006, [A&A](#), **452**, 875
- Reindl, N., Geier, S., Kupfer, T., et al. 2016, [A&A](#), **587**, A101
- Renzini, A., D’Antona, F., Cassisi, S., et al. 2015, [MNRAS](#), **454**, 4197
- Richard, J., Bacon, R., Blaizot, J., et al. 2019, [ArXiv e-prints](#) [arXiv:1906.01657]
- Rosenberg, A., Recio-Blanco, A., & García-Marín, M., 2004, [ApJ](#), **603**, 135
- Sahu, S., Subramaniam, A., Singh, G., et al. 2022, [MNRAS](#), **514**, 1122
- Sarajedini, A., Bedin, L. R., Chaboyer, B., et al. 2007, [AJ](#), **133**, 1658
- Schaffenroth, V., Pelisoli, I., Barlow, B. N., Geier, S., & Kupfer, T. 2022, [A&A](#), **666**, A182
- Schneider, D. 2022, PhD thesis, Friedrich-Alexander-Universität Erlangen-Nürnberg, Germany
- Swiegart, A. V. 2002, [Highlights Astron.](#), **12**, 292
- Tailo, M., Di Criscienzo, M., D’Antona, F., Caloi, V., & Ventura, P. 2016, [MNRAS](#), **457**, 4525
- Tremblay, P. E., & Bergeron, P. 2009, [ApJ](#), **696**, 1755
- Villanova, S., Piotto, G., & Gratton, R. G. 2009, [A&A](#), **499**, 755
- Villanova, S., Geisler, D., Piotto, G., & Gratton, R. G. 2012, [ApJ](#), **748**, 62
- Weilbacher, P. M., Palsa, R., Streicher, O., et al. 2020, [A&A](#), **641**, A28
- Yi, S. K. 2008, [ASP Conf. Ser.](#), **392**, 3

Appendix A: Additional material on SED fits

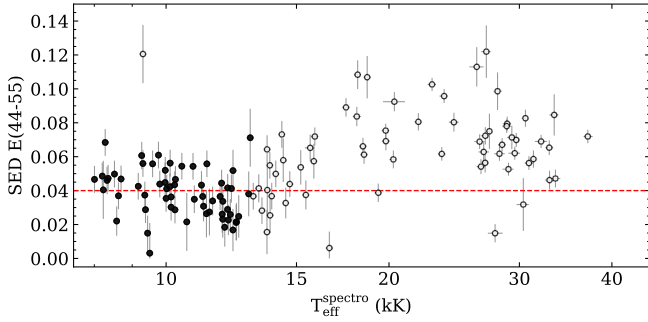


Fig. A.1. Reddening versus effective temperature for the stars in NGC 6752. Stars with T_{eff} below 13 kK (filled symbols) were used to derive the average $E(44-55)$, (dashed line).

Appendix A.1: Reddening estimate

We first attempted a simultaneous fit of T_{eff} and Θ in NGC 6752 while keeping the reddening fixed to $E(B-V) = 0.046$ mag (Gratton et al. 2005) but we found a clear trend between $T_{\text{eff}}^{\text{spec}}$ and $T_{\text{eff}}^{\text{SED}}$ among the cold stars. This is because both the reddening and T_{eff} affect the shape of the SED in a similar way for BHB stars. We therefore fixed T_{eff} to its spectroscopic value and left the reddening and Θ as free parameters. We obtained results as seen in Fig. A.1. In stars hotter than ~ 15 kK, we notice a clear increase in the reddening value with T_{eff} . This behavior is related to the discrepancy between $T_{\text{eff}}^{\text{spec}}$ and $T_{\text{eff}}^{\text{SED}}$ in the hot stars, which is discussed in the following subsection. Because the temperatures obtained from the spectra and the SED fits are in good agreement for stars cooler than 13 kK, we use the reddening values obtained from these stars to compute the average reddening. We proceeded in the same way for ω Cen.

The average reddening values obtained for both clusters, $E(44-55) = 0.04 \pm 0.01$ mag for NGC 6752 and $E(44-55) = 0.12 \pm 0.02$ mag for ω Cen, are in perfect agreement with the expected values from the literature (Harris, 2010 edition). We note here that, for $T_{\text{eff}} = 10\,000$ K, the extinction conversion $E(B-V)/E(44-55) = 0.976$ (Fitzpatrick et al. 2019). For ω Cen, we used the reddening map of Bellini et al. (2017b) to take into account differential reddening and therefore applied a correction to the reddening value of each star. However, these corrections are within ± 0.01 mag, which is relatively small.

Appendix A.2: Spectroscopic T_{eff} versus photometric T_{eff}

With the reddening fixed, we then performed a second run of SED fits where T_{eff} and Θ were the two free parameters as explained in Sect. 7. Here we compared the effective temperatures determined from the spectral fits with those obtained from SED fits. The results are shown in Fig. A.2. The temperatures derived from both methods are in good agreement up to ~ 15 kK. Above this temperature, the spectroscopic T_{eff} are generally hotter than the SED T_{eff} by 2–3 kK. For stars hotter than ~ 30 kK, neither method is expected to provide robust values. In the case of MUSE spectroscopy, the Paschen series disappears and few spectral lines are left to constrain the atmospheric parameters (see Figs. 4 and 5). In the case of the SED, the peak of the emitted flux moves to the FUV in the hottest stars, and the flux slope in the optical range loses its sensitivity to temperature changes. We note that the known reddening and F225W magnitudes in ω

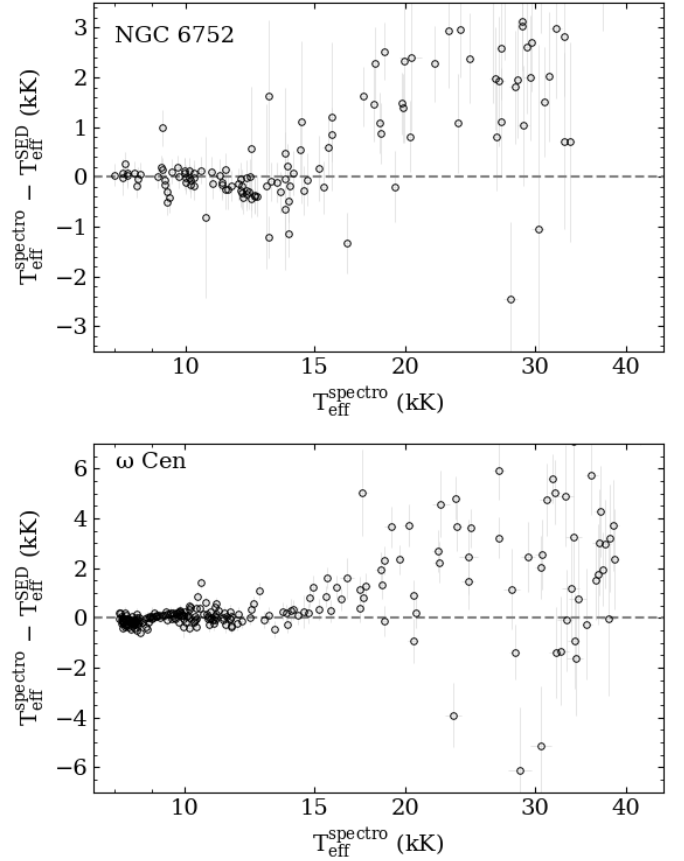


Fig. A.2. Difference in effective temperature between the spectroscopic and photometric fits for NGC 6752 (upper panel) and ω Cen (lower panel).

Cen are decisive for constraining T_{eff} from photometry in the hot objects.

For stars between ~ 15 – 30 kK, it is not clear which method provides the best T_{eff} . In Sect. 5.1, we see that the spectroscopic T_{eff} provide realistic temperatures for the M-jump, namely 18.6 kK and 19.5 kK in NGC 6752 and ω Cen, respectively. If we follow the same procedure, this time using the photometric effective temperatures, we obtain 17.2 kK and 17.1 kK for NGC 6752 and ω Cen. These temperatures are lower than expected from evolutionary models, which put the M-jump at 20–18 kK. The temperatures at the G-jump remain unchanged.

We also performed the SED fits for both clusters with T_{eff} fixed to the spectroscopic value, thus leaving Θ as the only free parameter. The resulting radii, luminosities, and masses are shown in Fig. A.3. In NGC 6752, we see that the stars hotter than 15 kK start to deviate from the predicted tracks; they are larger, more luminous, and less massive than expected. In ω Cen, the discrepancies in terms of radius and luminosity are less pronounced than for NGC 6752, but the mass discrepancy is stronger.

Why the spectroscopic T_{eff} of the hot stars ($T_{\text{eff}} \gtrsim 15$ kK) do not agree with that of their SED remains unclear to us. At this point, we cannot say which method provides the most accurate T_{eff} . However, for the cold stars, we have consistent results from both photometric and spectral fits, as well as a good agreement with theoretical prescriptions. This demonstrates that the SED fitting method is a powerful tool for analyzing A-BHB and B-BHB stars.

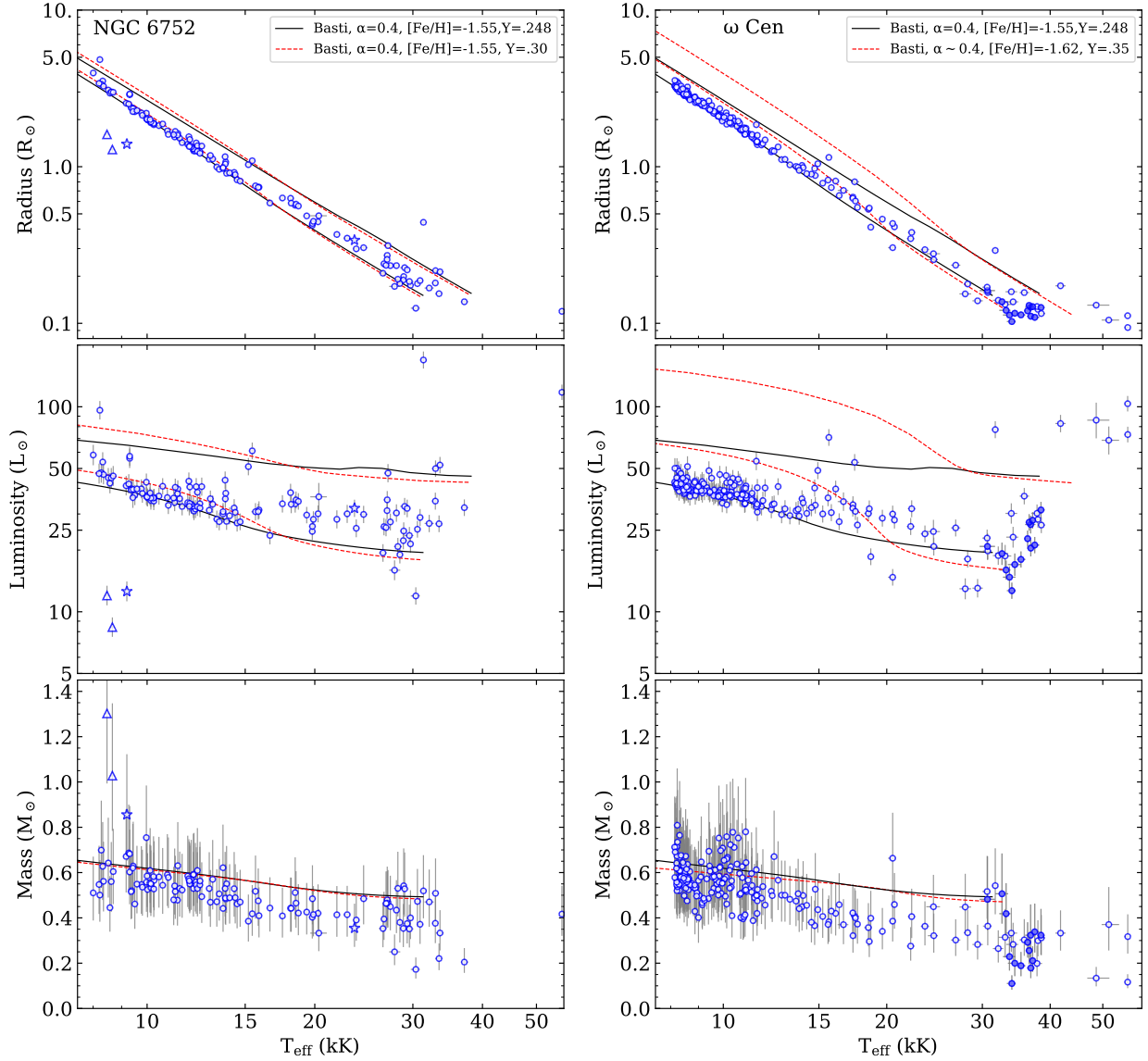


Fig. A.3. Radius, luminosity, and mass versus T_{eff} for the stars in NGC 6752 (left panels) and ω Cen (right panels). T_{eff} is obtained from the spectral fits and fixed to this value in the SED fitting process. The filled symbols in ω Cen indicate the He-rich (blue-hook) stars. We show the theoretical ZAHB and TAHB for He-normal and He-enriched models.

Appendix B: Description of the online tables

The results of our spectroscopic analysis of the MUSE spectra are only available online at CDS as Table B.1 and B.2 for NGC 6752 and ω Cen, respectively. We include in these tables columns with star identification numbers, coordinates, atmospheric parameters derived, and their uncertainties as described in Sect. 3.2, the number of individual spectra combined, and the S/N of the resulting spectra. We also add a column with alternative star names. We provide here the equation to convert the He abundances from fractional particle number (see Sect. 3.1) to number relative to hydrogen:

$$\log \frac{N(\text{He})}{N(\text{H})} = \log \frac{10^Y}{1 - 10^Y}, \quad (\text{B.1})$$

where

$$Y = \log \frac{N(\text{He})}{N(\text{tot})}. \quad (\text{B.2})$$

We note that this transformation is valid when $N(\text{H}) + N(\text{He}) \sim N(\text{tot})$.

The results of the SED fits are presented in four tables. The first two (Table B.3 and B.4, for NGC 6752 and ω Cen, respectively) present the results obtained when fitting θ and T_{eff} simultaneously. Along with the identification numbers of the stars, their coordinates, and their obtained parameters (T_{eff} , θ , radius, luminosity, and mass), we also list the magnitudes collected from the three catalogs we used (Nardiello et al. 2018; Bellini et al. 2017a; Anderson & van der Marel 2010). Finally, Tables B.5 and B.6 (for NGC 6752 and ω Cen, respectively) include the results of the SED fits when θ is the only free parameter and T_{eff} is fixed to the spectroscopic value.